NASA/TP–2016-219211

An Enriched Shell Finite Element for Progressive Damage Simulation in Composite Laminates

Mark W. McElroy
Langley Research Center, Hampton, Virginia

.

June 2016

NASA STI Program . . . in Profile

Since its founding, NASA has been dedicated to the advancement of aeronautics and space science. The NASA scientific and technical information (STI) program plays a key part in helping NASA maintain this important role.

The NASA STI program operates under the auspices of the Agency Chief Information Officer. It collects, organizes, provides for archiving, and disseminates NASA's STI. The NASA STI program provides access to the NTRS Registered and its public interface, the NASA Technical Reports Server, thus providing one of the largest collections of aeronautical and space science STI in the world. Results are published in both non-NASA channels and by NASA in the NASA STI Report Series, which includes the following report types:

- TECHNICAL PUBLICATION. Reports of completed research or a major significant phase of research that present the results of NASA Programs and include extensive data or theoretical analysis. Includes compilations of significant scientific and technical data and information deemed to be of continuing reference value. NASA counter-part of peer-reviewed formal professional papers but has less stringent limitations on manuscript length and extent of graphic presentations.

- TECHNICAL MEMORANDUM. Scientific and technical findings that are preliminary or of specialized interest, e.g., quick release reports, working papers, and bibliographies that contain minimal annotation. Does not contain extensive analysis.

- CONTRACTOR REPORT. Scientific and technical findings by NASA-sponsored contractors and grantees.

- CONFERENCE PUBLICATION. Collected papers from scientific and technical conferences, symposia, seminars, or other meetings sponsored or co-sponsored by NASA.

- SPECIAL PUBLICATION. Scientific, technical, or historical information from NASA programs, projects, and missions, often concerned with subjects having substantial public interest.

- TECHNICAL TRANSLATION. English-language translations of foreign scientific and technical material pertinent to NASA's mission.

Specialized services also include organizing and publishing research results, distributing specialized research announcements and feeds, providing information desk and personal search support, and enabling data exchange services.

For more information about the NASA STI program, see the following:

- Access the NASA STI program home page at http://www.sti.nasa.gov

- E-mail your question to help@sti.nasa.gov

- Phone the NASA STI Information Desk at 757-864-9658

- Write to:
  NASA STI Information Desk
  Mail Stop 148
  NASA Langley Research Center
  Hampton, VA 23681-2199

NASA/TP–2016-219211

An Enriched Shell Finite Element for Progressive Damage Simulation in Composite Laminates

Mark W. McElroy
Langley Research Center, Hampton, Virginia

National Aeronautics and
Space Administration

Langley Research Center
Hampton, Virginia 23681-2199

June 2016

Acknowledgment

Thank you to Dr. Nelson De Carvalho for his consultation and advice in support of this research.

The use of trademarks or names of manufacturers in this report is for accurate reporting and does not constitute an official endorsement, either expressed or implied, of such products or manufacturers by the National Aeronautics and Space Administration.

Available from:

NASA STI Program / Mail Stop 148
NASA Langley Research Center
Hampton, VA 23681-2199
Fax: 757-864-6500

Abstract

A formulation is presented for an enriched shell finite element capable of progressive damage simulation in composite laminates. The element uses a discrete adaptive splitting approach for damage representation that allows for a straightforward model creation procedure based on an initially low fidelity mesh. The enriched element is verified for Mode I, Mode II, and mixed Mode I/II delamination simulation using numerical benchmark data. Experimental validation is performed using test data from a delamination-migration experiment. Good correlation was found between the enriched shell element model results and the numerical and experimental data sets. The work presented in this paper is meant to serve as a first milestone in the enriched element's development with an ultimate goal of simulating three-dimensional progressive damage processes in multidirectional laminates.

1 Introduction

The use of lightweight composite materials in new aircraft designs is one means of increasing energy efficiency and decreasing operating costs compared to legacy aircraft constructed from traditional materials such as aluminum. A challenge with using composite materials is their susceptibility to brittle failure resulting from transverse loads such as impact [1]. Additionally, in-plane compressive loading after impact may result in further damage growth and eventual structural failure even if the initial impact damage itself was insignificant [2–4]. Therefore, for composite structures to be reliable and safe they must be designed and certified to survive some level of impact damage and subsequent compressive loading.

Certification of structural components is performed by testing or simulation. The latter is usually preferred, if it is possible, due to the lower relative cost. Currently, a lack of reliable and robust simulation tools for progressive damage in composite laminates results in a high reliance on testing for certification [5–7]. Reliable and cost effective simulation of progressive damage occurring during or after impact damage could potentially reduce the need for testing. Additionally, an efficient tool of this nature may allow for better component design early on and prevent costly redesigns.

Some typical causes of impact loads are hail, bird strike, tool drops, or baggage cart collisions. Tool drops and baggage cart collisions fall into the category of low-velocity impact. Low-velocity impact damage can be particularly concerning because damage is often not visible externally, but can be significant in the interior of a laminate. This is commonly referred to as barely visible impact damage (BVID). An example of BVID is shown in a cross section of a laminate in Figure 1 [8]. Here, the damage is not visible externally, but internally is extensive and consists of multiple delaminations at different ply interfaces connected via matrix cracks. A numerical simulation tool applicable to low-velocity impact or compression after impact (CAI) must be capable of capturing the physics within a progressive damage process that results in this type of damage pattern.

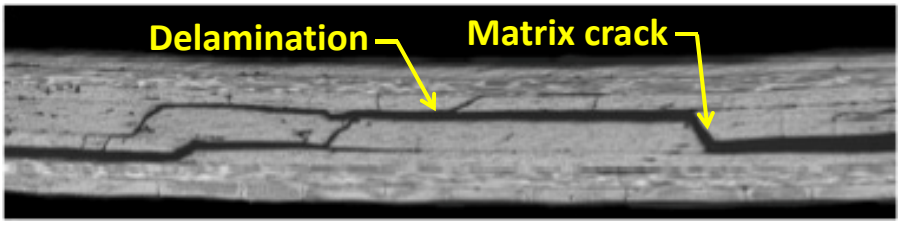

Figure 1. Example of barely visible impact damage [8].

1.1 Background

Study of impact loading and damage prediction in composite laminates dates back to the 1970s [9]. Much of the early work in this field was experimental and directed towards observing the nature of damage that forms during low-velocity impact [10–12]. Of particular note is the study by Choi et al. where impact testing was performed on cross-ply specimens in order to render the physical response effectively into two dimensions (2D). In doing this, the failure mechanisms could be better observed and understood. Choi et al.'s work showed the fundamental process that occurs in a low-velocity impact, illustrated in Figure 2, where (1) matrix cracks first form, either in the tensile region due to bending, or elsewhere due to transverse shear (depending on layup) and (2) matrix cracks grow out-of-plane until a ply interface of dissimilar fiber orientation is reached where delamination can initiate.

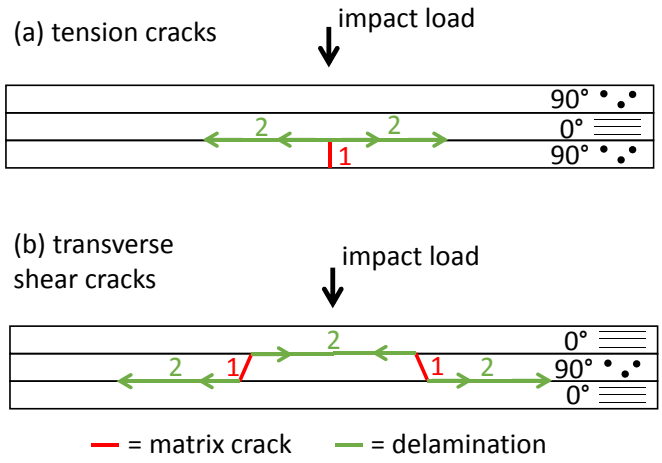

Figure 2. Example of typical impact damage as observed by Choi et al. [12] with sequence of events identified by number.

Other research in this time frame dealt with development of analytical predictive tools, including prediction of impact force response [13–16]. In some cases, analytical tools included not only impact force response, but also a means to predict the onset and extent of damage [17–21]. Analytical models such as this are useful in certain design applications; however, they have limited ability to address problems

that involve complex damage processes consisting of many interacting failure modes or when dealing with structures that have irregular geometry and/or boundary conditions. One means to address these types of complexities is through use of finite element models.

Finite element (FE) simulation of progressive damage in laminates from low-velocity impact began in the 1990s [22–24]. Since then, progressive damage simulation in laminates has advanced considerably due partially to advances in computational technology, but also due to advances in numerical simulation techniques. Two fracture based techniques, cohesive zone (CZ) and the Virtual Crack Closure Technique (VCCT), are used commonly for crack growth simulation in FE models. CZ modeling was initially used to simulate crack growth in metals [25]. An initial cohesive FE formulation was presented by Beer in 1985 [26], and has since seen many enhancements for use in laminate damage simulations, including accommodation of mode-mixity [27,28]. An alternative technique to CZ modeling is VCCT [29]. First presented by Rybicki [30, 31], VCCT was first used in the context of damage prediction in laminates as early as the late 1970s and 1980s [32, 33].

CZ modeling and VCCT each have advantages and disadvantages. CZ models inherently have solution convergence difficulties and also generally require a very fine mesh [34]. On the other hand, initiation and growth are both inherently built into the technique, which is not the case with VCCT. VCCT requires that an initial flaw exists in the model; however, VCCT can accurately predict crack growth with a much coarser mesh. Additionally, the convergence issues seen with CZ models are not present in VCCT. Both CZ and VCCT are used for laminate damage simulation in current state-of-the-art damage models [35].

Simulating a progressive damage process of the types seen in Figures 1 and 2, requires the consideration of interacting transverse matrix cracks and delaminations. Finite element models aimed at capturing this type of behavior in detail became possible only when numerical and computational tools became more robust [35]. Many FE models began to combine several damage simulation techniques into the same model. Continuum damage mechanics (CDM) [36–38], based on degradation of element material properties in an area of damage, and the eXtended Finite Element Method (XFEM) [39, 40], based on a discrete discontinuity in a mesh displacement field, have emerged as two approaches used in FE modeling in conjunction with CZ and VCCT techniques.

Many state-of-the-art simulation models for progressive damage in laminates are combinations and variations of the techniques mentioned above. Additionally, most models fall into one of two categories where intralaminar damage such as fiber failure and matrix cracking are simulated with CDM [41–43] or where the intralaminar damage is simulated discretely [44–46]. The use of CZ approach for delamination failure is common in both of these methods, although VCCT has also been used [47, 48]. The two approaches have also been combined such that fiber failure is simulated with CDM, and intralaminar matrix cracks and delamination are modeled discretely [49, 50].

Finite element models that use combinations of CDM, XFEM, VCCT, and CZs for progressive damage simulation tend to be high fidelity in nature, consisting of a level of mesh discretization of at least one element per ply. Model fidelity is

typically high for two main reasons. First, a fine mesh with at least one element per ply allows for detailed stress and strain through the laminate thickness in each ply to be calculated and used in a criterion to predict initiation and propagation of damage. Second, representation of a three-dimensional damage pattern, as dictated by the prediction, is intuitive in a mesh that is also three-dimensional. A disadvantage of high fidelity meshes, in general, is that they are very inefficient, as a large amount of information is determined throughout the entire model when this level of detail is only needed at locations where a damage process is occurring.

Laminates used in structures can have dozens of plies or more, so use of models that rely on a discretization level of at least one element per ply in the thickness direction is limited not only by their computational demand, but also by the complexity of the process required by the user to create and verify a model. Current numerical damage simulation techniques using finite elements have yet to be demonstrated to be accurate in a consistent and general manner for problems beyond small structures with simple layups that undergo simple damage processes (i.e., simple relative to a realistic scenario where a laminate may have dozens of plies with damage propagating three-dimensionally throughout the entire layup) [35, 51]. Hence, more efficient models and simulation techniques that demand less computationally, as well as require less time and expertise from the user, are desirable. Use of shell element models may offer an alternative.

1.2 Shell elements in progressive damage simulation

Shell elements have long been used by industry and have proven to be a cost effective analysis tool, albeit, for problems less complex than laminate damage simulation. Shell element models are computationally efficient and generally require less training and time for an analyst to use when compared to a high fidelity solid element model. Use of shell element models for laminate damage simulation, however, introduces a number of challenges, including prediction and representation of transverse matrix cracks and delaminations at multiple interfaces.

Previously, use of shell elements for progressive damage simulation has consisted of either a global-local approach [52], where the actual damage simulation takes place in a high fidelity region attached to an otherwise low fidelity model, or by stacking layers of shell elements to form a laminate [53–57]. In the stacked shell approach, independent layers of shell elements are defined and connected across ply interfaces in a laminate. If delamination at a specific ply interface is of interest, a mesh may consist of two layers of shell elements, one on either side of the ply interface location. The two layers can be connected by a CZ or by rigid links and delamination growth is predicted with a cohesive law or VCCT, respectively.

Wang et al. [58, 59] studied the use of VCCT for delamination prediction between stacked shell elements. This work, along with a related study [60], indicate that mixed-mode energy release rate can be calculated using shell elements; however, continued mesh refinement may not result in converged values in some cases. Similarly, in bimaterial crack tip interfaces, energy release rate component divergence is observed with mesh refinement near the crack tip/delamination front when using VCCT with any element type. Previous work indicated that this non-convergence

may be avoided by establishing a minimum mesh size based on the ratio of incremental crack growth length in the mesh to element thickness, $\Delta a/h$ [61].

An inherent disadvantage of the two-layer stacked shell models is that the delamination interface must be predefined, thereby limiting the model's utility as a general predictive tool. Furthermore, by restricting the delamination to a single ply interface location, multiple delaminations, or delamination and matrix crack interaction, is not possible. One means to avoid this is to model many, or all, interfaces in the mesh by creating an independent layer of shells for every ply and stacking all of the layers to form the laminate. This type of approach, however, begins to share some of the same drawbacks mentioned for high fidelity solid element models, namely lengthy and complex model preparation and high computational demand.

Ideally, in terms of computational efficiency; ease of use; and predictive utility, a thin laminate plate would be modeled as a single layer of shell elements in which delaminations could form and propagate at any location in the layup. This type of approach can be thought of as having adaptive fidelity in that the model is defined initially in low fidelity (one shell element thick) and remains in this state everywhere except locally where delamination occurs and multiple layers are required as dictated by a damage prediction criteria throughout an analysis solution. Effectively, in the local damaged regions, the stacked shell technique described previously is used.

Simulation models based on shell elements that use adaptive fidelity have been proposed and studied only recently. Larsson presented a shell element in 2004 [62] that treats delaminations as an in-plane discontinuity in the displacement field in a shell formulation and uses a cohesive zone to predict growth. Similarly, Brouzoulis et al. [63–65] have developed a shell element that uses XFEM and cohesive zones to simulate growth of multiple delaminations and transverse matrix cracks in a shell element. Their work is ongoing but, while showing promise, has not yet advanced to the point of being able to simulate a realistic and practical progressive damage problem such as low-velocity impact.

Since the development of XFEM, several variations and improvements have been proposed, including Regularized-XFEM [66] and the Phantom Node Method [67]. A more recent study was published on the newly introduced Floating Node Method (FNM) [68]. The FNM's technique for numerical discrete damage representation has an inherent simplicity, compared to the other techniques, that makes it straightforward to implement and easy to modify and customize. Additionally, it offers some advantages related to element crack mapping and the integration procedure [68].

When using the FNM to introduce mesh discontinuities representative of damage growth, a crack propagation technique is needed. VCCT offers an efficient numerical solution procedure and does not have convergence difficulties and mesh refinement requirements that are associated with the use of cohesive zones. Studies have shown that when using a transverse shear deformable shell element, mixed-mode energy release rates can be calculated accurately with VCCT [48,57,60,69,70]. Furthermore, it was shown that VCCT could be successfully combined with the FNM to model crack growth [47], though this was not using shell elements. Complications can arise when using VCCT in scenarios where a delamination propagation direction is not aligned with the mesh. Though this difficulty has been studied and solutions have been proposed that can generate accurate behavior [71–74], it remains an additional

challenge for any numerical implementation.

The ability to predict transverse cracks that form adjacent to or along side of delaminations in shell models has received little attention in the past as it is seemingly unnatural to consider out-of-plane damage features in planar elements. This damage mechanism has been described as "delamination-migration" [75]. Studies have shown that the occurrence of delamination-migration in a crossply specimen can be described as a function of the sign of the in-plane shear force at the delaminated interface between the upper and lower groups of intact plies around a delamination crack front [75,76]. Additionally, similar work suggests that delamination migration may be able to be predicted using orthogonal components of in-plane (i.e., Mode II and Mode III) energy release rates [77–80]. Drawing from conclusions reached in this selection of work, in-plane energy release rate components determined using VCCT along with the shear force sign between upper and lower regions of a delamination front may be used to determine the preferential growth direction in three-dimensional space of the delamination. This information could then be used as the basis for a delamination-migration criteria.

1.3 Objective

The goal of this paper is to present the formulation and initial verification and validation of a novel enriched shell element capable of progressive damage simulation in composite laminates. Specifically, the capability to predict mixed-mode delaminations and delamination-migration is included. The element enrichment allows for adaptive mesh fidelity in which a single element splits into two subregions only as required locally, to model an evolving damage process. At any location in the model where damage does not occur, the original discretization remains unaffected and a single shell element is used to represent the entire laminate thickness as defined in the beginning of the analysis. This capability is achieved using the Floating Node Method to discretely represent a delamination in the mesh and VCCT to predict its growth. The element is coded as a user-subroutine in Abaqus 6.14/Standard® [81]. Details concerning the use of VCCT in conjunction with shell elements, mesh dependency of the solution, and out-of-plane damage formation are investigated. This study serves only as the first milestone of the enriched shell element's development, for which the ultimate goal is to be able to simulate a progressive damage process similar to that of low-velocity impact or compression-after-impact.

2 Element Formulation

Much of the element formulation presented here is based on information presented in [82] for a laminate Mindlin shell element. Using this formulation, and after addressing shear locking and applying layerwise shear correction factors, the element is suitable for thick and thin (i.e., transverse shear or bending dominated) shells. The element is enriched with the Floating Node Method and uses the Virtual Crack Closure Technique (VCCT) to perform discrete laminate damage simulations. This section demonstrates how the element stiffness matrix, $\mathbf{K}^{(e)}$, for the enriched shell, is obtained using the well known expression for a linear elastic element

$$\mathbf{K}^{(e)} = \int_{xyz} \mathbf{B}^T \mathbf{D} \mathbf{B} dV \tag{1}$$

where $\mathbf{B}$ is the strain-displacement matrix and $\mathbf{D}$ is the constitutive material matrix.

2.1 Mindlin Shell Element

A four node shell element with five degrees-of-freedom (DOF) per node is shown in three-dimensional space in Figure 3. The node and DOF labels as defined in Figure 3 are used henceforth. The prime superscript refers to a local (i.e., element) coordinate system which may be oriented arbitrarily in global three-dimensional space. The element displacement field, in three orthogonal components, is described by

$$u'(x', y', z') = u'_o(x', y') - z'\theta_x(x', y') \tag{2a}$$
$$v'(x', y', z') = v'_o(x', y') - z'\theta_y(x', y') \tag{2b}$$
$$w'(x', y', z') = w'_o(x', y') \tag{2c}$$

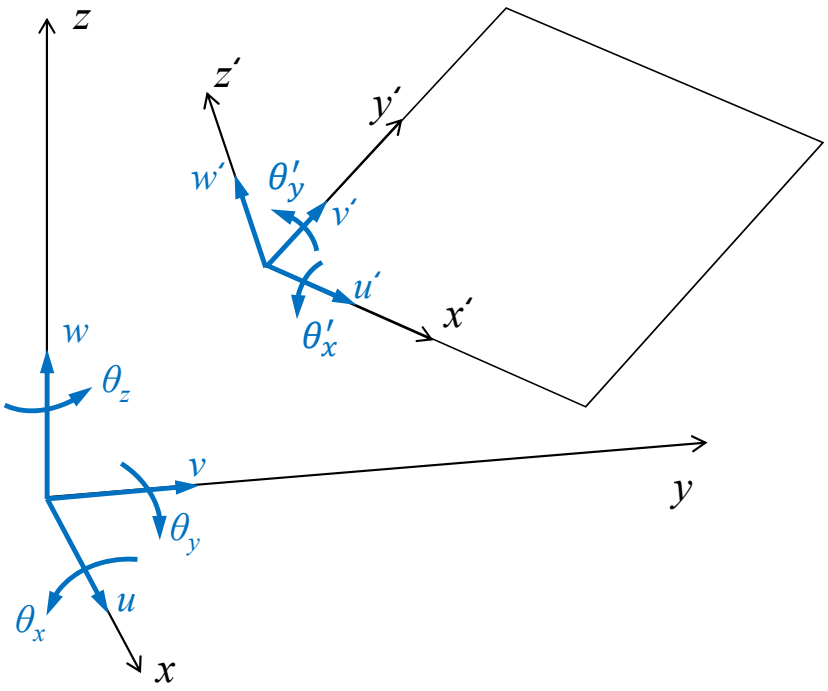

Figure 3. Shell element schematic.

If the element displacement field is discretized at the node locations, as in a typical finite element model solution, the nodal displacements, $\mathbf{a}_i$, can be interpolated at a given location in the element (x', y', z') using shape functions. For an element with four nodes, the displacement field is described by

$$\begin{bmatrix} u'(x',y',z') \\ v'(x',y',z') \\ w'(x',y',z') \end{bmatrix} = \mathbf{N}\mathbf{a}^{(e)}$$

$$= \sum_{i=1}^{4} \mathbf{N}_i \mathbf{a}_i = \begin{bmatrix} \mathbf{N}_1 & \mathbf{N}_2 & \mathbf{N}_3 & \mathbf{N}_4 \end{bmatrix} \begin{bmatrix} \mathbf{a}_1 \\ \mathbf{a}_2 \\ \mathbf{a}_3 \\ \mathbf{a}_4 \end{bmatrix} \tag{3}$$

where i = node number,

$$\mathbf{a}_i = \begin{bmatrix} u'_i \\ v'_i \\ w'_i \\ \theta'_{xi} \\ \theta'_{yi} \end{bmatrix} \tag{4}$$

and

$$\mathbf{N}_i = \begin{bmatrix} N_i & 0 & 0 & 0 & 0 \\ 0 & N_i & 0 & 0 & 0 \\ 0 & 0 & N_i & 0 & 0 \\ 0 & 0 & 0 & N_i & 0 \\ 0 & 0 & 0 & 0 & N_i \end{bmatrix} \tag{5}$$

Standard linear shape functions are used and defined as

$$N_1 = 1/4(1 - x')(1 - y') \tag{6a}$$
$$N_2 = 1/4(1 + x')(1 - y') \tag{6b}$$
$$N_3 = 1/4(1 + x')(1 + y') \tag{6c}$$
$$N_4 = 1/4(1 - x')(1 + y') \tag{6d}$$

The element strain field, $\boldsymbol{\varepsilon}$, may be divided into a planar component and a transverse shear component, $\boldsymbol{\varepsilon}_p$ and $\boldsymbol{\varepsilon}_s$, respectively. Assuming plane stress conditions (i.e., $\sigma'_z = 0$) the strain field is defined as

$$\boldsymbol{\varepsilon} = \begin{bmatrix} \boldsymbol{\varepsilon}_p \\ \hdashline \boldsymbol{\varepsilon}_s \end{bmatrix} = \begin{bmatrix} \varepsilon_x \\ \varepsilon_y \\ \gamma_{xy} \\ \hdashline \gamma_{xz} \\ \gamma_{yz} \end{bmatrix} = \begin{bmatrix} \partial u'/\partial x' \\ \partial v'/\partial y' \\ \partial u'/\partial y' + \partial v'/\partial x' \\ \hdashline \partial u'/\partial z' + \partial w'/\partial x' \\ \partial v'/\partial z' + \partial w'/\partial y' \end{bmatrix}$$

$$= \begin{bmatrix} \partial u'_o/\partial x' \\ \partial v'_o/\partial y' \\ \partial u'/\partial y' + \partial v'/\partial x' \\ \hdashline 0 \\ 0 \end{bmatrix} + \begin{bmatrix} -z'(\partial \theta'_x/\partial x') \\ -z'(\partial \theta'_y/\partial y') \\ -z'(\partial \theta'_x/\partial y' + \partial \theta'_y/\partial x') \\ \hdashline \partial w'_o/\partial x' - \theta'_x \\ \partial w'_o/\partial y' - \theta'_y \end{bmatrix} \tag{7}$$

It is convenient to transform and expand the strain vector, $\boldsymbol{\varepsilon}$, in equation 7 to a generalized form, $\boldsymbol{\varepsilon}^{(g)}$, for which components resulting from membrane, bending, and transverse shear deformations are segregated as $\boldsymbol{\varepsilon}_m$, $\boldsymbol{\varepsilon}_b$, and $\boldsymbol{\varepsilon}_s$, respectively. The transformation is useful because, if desired, different stiffness integration techniques and/or corrections can be made for each deformation mode independently from the others. Generalized strain is related to strain by

$$\boldsymbol{\varepsilon} = \mathbf{S}\boldsymbol{\varepsilon}^{(g)} \tag{8}$$

where

$$\mathbf{S} = \begin{bmatrix} 1 & 0 & 0 & -z' & 0 & 0 & 0 & 0 \\ 0 & 1 & 0 & 0 & -z' & 0 & 0 & 0 \\ 0 & 0 & 1 & 0 & 0 & -z' & 0 & 0 \\ 0 & 0 & 0 & 0 & 0 & 0 & 1 & 0 \\ 0 & 0 & 0 & 0 & 0 & 0 & 0 & 1 \end{bmatrix} \tag{9}$$

and $\boldsymbol{\varepsilon}^{(g)}$ is given by

$$\boldsymbol{\varepsilon}^{(g)} = \begin{bmatrix} \boldsymbol{\varepsilon}_m^{(g)} \\ \hdashline \boldsymbol{\varepsilon}_b^{(g)} \\ \hdashline \boldsymbol{\varepsilon}_s^{(g)} \end{bmatrix} = \sum_{i=1}^{4} \begin{bmatrix} (\partial N_i/\partial x')u'_{oi} \\ (\partial N_i/\partial y')v'_{oi} \\ \hdashline (\partial N_i/\partial y')u'_{oi} + (\partial N_i/\partial x')v'_{oi} \\ \hdashline (\partial N_i/\partial x')\theta'_{xi} \\ (\partial N_i/\partial y')\theta'_{yi} \\ \hdashline (\partial N_i/\partial y')\theta'_{xi} + (\partial N_i/\partial x')\theta'_{yi} \\ \hdashline (\partial N_i/\partial x')w'_{oi} - N_i\theta'_{xi} \\ (\partial N_i/\partial y')w'_{oi} - N_i\theta'_{yi} \end{bmatrix} \tag{10}$$

where i is equal to node number.

A relation between the generalized strains, $\boldsymbol{\varepsilon}^{(g)}$, and the nodal displacements, $\mathbf{a}_i$, is established using the strain-displacement matrix, $\mathbf{B}$, as

$$\boldsymbol{\varepsilon}^{(g)} = \sum_{i=1}^{4} \mathbf{B}_i\mathbf{a}_i = \begin{bmatrix} \mathbf{B}_1 & \mathbf{B}_2 & \mathbf{B}_3 & \mathbf{B}_4 \end{bmatrix} \begin{bmatrix} \mathbf{a}_1 \\ \mathbf{a}_2 \\ \mathbf{a}_3 \\ \mathbf{a}_4 \end{bmatrix} \tag{11}$$

The membrane, bending, and transverse shear components of $\mathbf{B}$ ($\mathbf{B}_i^{(m)}$, $\mathbf{B}_i^{(b)}$, and $\mathbf{B}_i^{(s)}$, respectively) can be segregated and $\mathbf{B}_i$ can be expressed as

$$\mathbf{B}_i = \begin{bmatrix} \mathbf{B}_i^{(m)} \\ \hdashline \mathbf{B}_i^{(b)} \\ \hdashline \mathbf{B}_i^{(s)} \end{bmatrix} \tag{12}$$

where

$$\mathbf{B}_i^{(m)} = \begin{bmatrix} (\partial N_i/\partial x') & 0 & 0 & 0 & 0 \\ 0 & (\partial N_i/\partial y') & 0 & 0 & 0 \\ (\partial N_i/\partial y') & (\partial N_i/\partial x') & 0 & 0 & 0 \end{bmatrix} \tag{13}$$

$$\mathbf{B}_i^{(b)} = \begin{bmatrix} 0 & 0 & 0 & (\partial N_i/\partial x') & 0 \\ 0 & 0 & 0 & 0 & (\partial N_i/\partial y') \\ 0 & 0 & 0 & (\partial N_i/\partial y') & (\partial N_i/\partial x') \end{bmatrix} \tag{14}$$

$$\mathbf{B}_i^{(s)} = \begin{bmatrix} 0 & 0 & (\partial N_i/\partial x') & -N_i & 0 \\ 0 & 0 & (\partial N_i/\partial y') & 0 & -N_i \end{bmatrix} \tag{15}$$

Classical laminate theory is used to determine the constitutive material matrix, $\mathbf{D}$, for a composite section consisting of multiple orthogonal plies with varying fiber orientations. For a single ply with a fiber orientation, β, that is aligned with the x'-axis in the element coordinate system (i.e., β=0°), the constitutive in-plane and transverse shear material matrices, $\mathbf{D}^{(p)}$ and $\mathbf{D}^{(s)}$, respectively, are defined as

$$\mathbf{D}^{(p)} = \begin{bmatrix} E_1/(1-\nu_{12}\nu_{21}) & E_2\nu_{12}/(1-\nu_{12}\nu_{21}) & 0 \\ & E_2/(1-\nu_{12}\nu_{21}) & 0 \\ sym. & & G_{12} \end{bmatrix} \tag{16}$$

and

$$\mathbf{D}^{(s)} = \begin{bmatrix} G_{13} & 0 \\ 0 & G_{23} \end{bmatrix} \tag{17}$$

where E_i and G_{ij} are the material Young's and shear moduli, respectively, and ν_{ij} are the Poisson's ratios. In equations 16 and 17, the subscripts 1, 2, and 3, refer to the fiber, in-plane normal-to-fiber, and out-of-plane normal-to-fiber directions, respectively. For plies where the fiber orientation, β, is non-zero, $\mathbf{D}^{(p)}$ and $\mathbf{D}^{(s)}$ should be rotated about the element z'-axis using transformation matrices $\bar{\mathbf{T}}_1$ and $\bar{\mathbf{T}}_2$ to obtain the material matrix. The rotated ply level constitutive material matrices, $\bar{\mathbf{D}}^{(p)}$ and $\bar{\mathbf{D}}^{(s)}$, are determined by

$$\bar{\mathbf{D}}^{(p)} = \bar{\mathbf{T}}_1^T \mathbf{D}^{(p)} \bar{\mathbf{T}}_1 \tag{18a}$$

$$\bar{\mathbf{D}}^{(s)} = \bar{\mathbf{T}}_2^T \mathbf{D}^{(s)} \bar{\mathbf{T}}_2 \tag{18b}$$

where

$$\bar{\mathbf{T}}_1 = \begin{bmatrix} \cos^2(\beta) & \sin^2(\beta) & \cos(\beta)\sin(\beta) \\ \sin^2(\beta) & \cos^2(\beta) & -\cos(\beta)\sin(\beta) \\ -2\cos(\beta)\sin(\beta) & 2\cos(\beta)\sin(\beta) & \cos^2(\beta)-\sin^2(\beta) \end{bmatrix} \tag{19}$$

and

$$\bar{\mathbf{T}}_2 = \begin{bmatrix} \cos(\beta) & \sin(\beta) \\ -\sin(\beta) & \cos(\beta) \end{bmatrix} \tag{20}$$

The rotated shear matrix, $\bar{\mathbf{D}}^{(s)}$, should be further modified by applying shear correction factors, c_{11} and c_{22}. The shear correction factors, discussed in Section 2.2, are applied and a shear material matrix, $\bar{\mathbf{D}}^{(scf)}$, that is both rotated and includes shear corrections is defined as

$$\bar{\mathbf{D}}^{(scf)} = \begin{bmatrix} c_{11}\bar{D}_{11}^{(s)} & \bar{D}_{12}^{(s)} \\ \bar{D}_{21}^{(s)} & c_{22}\bar{D}_{22}^{(s)} \end{bmatrix} \tag{21}$$

Equations 16 and 17 are used in integrations along the z'-axis to generate homogenized laminate level material matrices for membrane ($\mathbf{D}^{(m)}$), membrane-bending coupling ($\mathbf{D}^{(mb)}$), bending ($\mathbf{D}^{(b)}$), and shear ($\mathbf{D}^{(s)}$) deformation behavior. The material matrices can be obtained using the following equations

$$\mathbf{D}^{(m)} = \int_{-h/2}^{h/2} \bar{\mathbf{D}}^{(p)} dz' = \sum_{k=1}^{n} t_k \bar{\mathbf{D}}_k^{(p)} \tag{22a}$$

$$\mathbf{D}^{(mb)} = -\int_{-h/2}^{h/2} z' \bar{\mathbf{D}}^{(p)} dz' = -\sum_{k=1}^{n} t_k \bar{z}_k \bar{\mathbf{D}}_k^{(p)} \tag{22b}$$

$$\mathbf{D}^{(b)} = \int_{-h/2}^{h/2} z'^2 \bar{\mathbf{D}}^{(p)} dz' = \sum_{k=1}^{n} \frac{1}{3}\left[z_{k+1}^3 - z_k^3\right] \bar{\mathbf{D}}_k^{(p)} \tag{22c}$$

$$\mathbf{D}^{(s)} = \int_{-h/2}^{h/2} \bar{\mathbf{D}}^{(scf)} dz' = \sum_{k=1}^{n} t_k \bar{\mathbf{D}}_k^{(s)} \tag{22d}$$

where k is the ply number and z_k, t_k, h, and $\bar{z}_k$ are thickness measures of the layup as defined in Figure 4. The constitutive material matrix, $\mathbf{D}$, for a laminate is given as

$$\mathbf{D} = \begin{bmatrix} \left[\mathbf{D}^{(m)}\right]_{3\times3} & \left[\mathbf{D}^{(mb)}\right]_{3\times3} & \left[\mathbf{0}\right]_{3\times2} \\ \left[\mathbf{D}^{(mb)}\right]_{3\times3} & \left[\mathbf{D}^{(b)}\right]_{3\times3} & \left[\mathbf{0}\right]_{3\times2} \\ \left[\mathbf{0}\right]_{2\times3} & \left[\mathbf{0}\right]_{2\times3} & \left[\mathbf{D}^{(s)}\right]_{2\times2} \end{bmatrix} \tag{23}$$

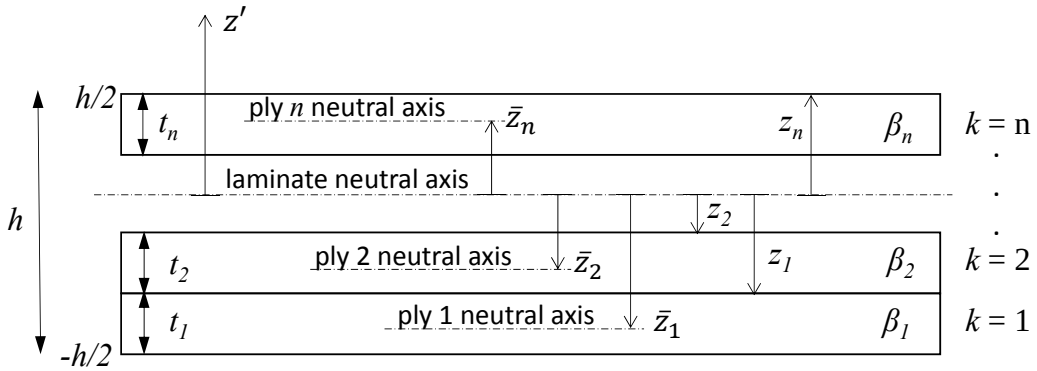

Figure 4. Laminate schematic (k = ply number, n = total number of plies, and β = ply orientation).

2.2 Shear correction factors

Shear correction factors in equation 21, c_{11} and c_{22}, are determined for each ply, k, using a method presented by Laitinen et al. [83]. Based on work by Vlachoutis [84], Laitinen et al.'s method is applicable to a general laminate of n plies with each having an arbitrary orientation, β. The method is based on determining the ratio of strain energy assuming transverse shear strain is constant and the strain energy assuming transverse shear strain has a parabolic distribution. This technique assumes cylindrical bending and determines the shear correction factors as a function of ply location in the layup and ply fiber angle. The shear correction factors for a ply are given by

$$c_{\psi\psi} = \frac{R_\psi^2}{d_\psi I_\psi} \qquad \psi = 1, 2 \tag{24}$$

where ψ is the direction in the laminate plane (i.e., 1 or 2). Laitinen defines R_ψ, d_ψ, and I_ψ for a laminate containing n layers as

$$R_\psi = \frac{1}{3}\sum_{k=1}^{n} \bar{Q}_{\psi\psi}^{(k)}\Big[(z_k - \bar{z}_{n\psi})^3 - (z_{k-1} - \bar{z}_{n\psi})^3\Big] \tag{25}$$

$$d_\psi = \sum_{k=1}^{n} \bar{Q}_{\delta\delta}^{(k)}(z_k - z_{k-1}) \qquad \delta = \psi + 3 \tag{26}$$

$$I_\psi = \sum_{k=1}^{n} \int_{z_{k-1}}^{z_k} \frac{g_\psi^2(z')}{\bar{Q}_{\delta\delta}^{(k)}} dz' \tag{27}$$

where

$$g_\psi(z') = -\frac{1}{2}\sum_{k=1}^{n_{k-1}} \Big(\bar{Q}_{\psi\psi}^{(k)}\Big[(z_k - \bar{z}_{n\psi})^2 - (z_{k-1} - \bar{z}_{n\psi})^2\Big] - \frac{1}{2}\bar{Q}_{\psi\psi}^{(k)}\Big[(z' - \bar{z}_{n\psi})^2 - (z_{n_k} - \bar{z}_{n\psi})^2\Big]\Big) \tag{28}$$

and

$$\bar{z}_{n\psi} = \frac{\frac{1}{2}\sum_{k=1}^{n} \bar{Q}_{\psi\psi}^{(k)}\big(z_k^2 - z_{k-1}^2\big)}{\bar{Q}_{\psi\psi}^{(k)}(z_k - z_{k-1})} \tag{29}$$

In equations 25-29, n = total number of plies, n_k = the current ply, and $\bar{Q}$ is defined for each ply, k, as

$$\bar{\mathbf{Q}} = \begin{bmatrix} \bar{\mathbf{D}}^{(p)} & \mathbf{0} \\ \mathbf{0} & \bar{\mathbf{D}}^{(scf)} \end{bmatrix} \tag{30}$$

2.3 Shear Locking

Mindlin shell elements that have a slender aspect ratio are subject to shear locking. This inaccuracy is the result of transverse shear terms dominating the stiffness matrix as the element thickness goes to zero (i.e., a slender aspect ratio). In practice, this may result in overly stiff elements under bending dominated deformations. Onate et al. present a methodology to overcome shear locking based on an assumed shear strain distribution that results in an element which is accurate in bending for thick and thin shells [85]. The following is a description of how to apply the methodology. For an element in its natural coordinate system, as shown in Figure 5, the transverse shear strains are assumed to follow a linear distribution in the (ξ,η) coordinate system as $\gamma_\xi = \alpha_1 + \alpha_2\eta$ and $\gamma_\eta = \alpha_3 + \alpha_4\xi$. In matrix form, this can be expressed as

$$\begin{bmatrix} \gamma_\xi \\ \gamma_\eta \end{bmatrix} = \begin{bmatrix} 1 & \eta & 0 & 0 \\ 0 & 0 & 1 & \xi \end{bmatrix} \begin{bmatrix} \alpha_1 \\ \alpha_2 \\ \alpha_3 \\ \alpha_4 \end{bmatrix} \tag{31}$$

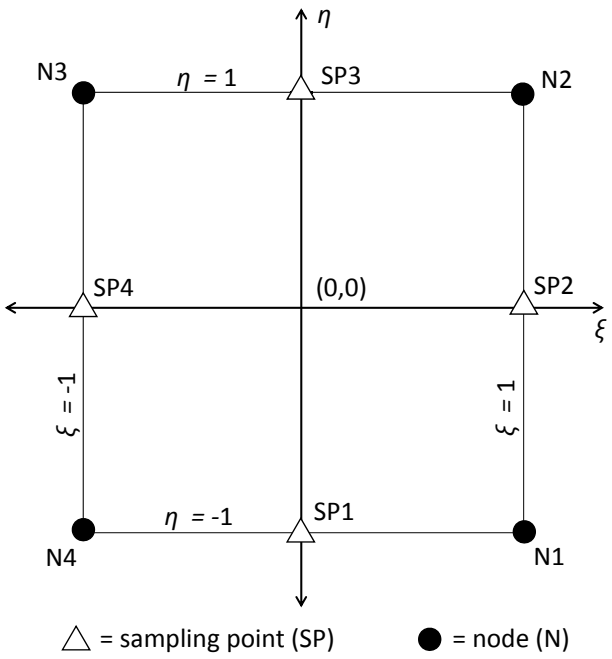

Figure 5. Element in natural coordinates.

The 2×4 coefficient matrix in equation 31 will be designated as **A**. The α parameters can be determined by sampling tangential transverse shear strains at the edges of an element at four locations (0,-1), (1,0), (0,1), and (-1,0) identified in Figure 5

as sample points. The shear strain at the four sample points is given by

$$\gamma^{(1)} = \alpha_1 + \alpha_2\eta^{(1)} = \alpha_1 - \alpha_2 \tag{32a}$$

$$\gamma^{(2)} = \alpha_3 + \alpha_4\xi^{(2)} = \alpha_3 + \alpha_4 \tag{32b}$$

$$\gamma^{(3)} = \alpha_1 + \alpha_2\eta^{(3)} = \alpha_1 + \alpha_2 \tag{32c}$$

$$\gamma^{(4)} = \alpha_3 + \alpha_4\xi^{(4)} = \alpha_3 - \alpha_4 \tag{32d}$$

or in matrix form as

$$\begin{bmatrix} \gamma^{(1)} \\ \gamma^{(2)} \\ \gamma^{(3)} \\ \gamma^{(4)} \end{bmatrix} = \begin{bmatrix} 1 & -1 & 0 & 0 \\ 0 & 0 & 1 & 1 \\ 1 & 1 & 0 & 0 \\ 0 & 0 & 1 & -1 \end{bmatrix} \begin{bmatrix} \alpha_1 \\ \alpha_2 \\ \alpha_3 \\ \alpha_4 \end{bmatrix} \tag{33}$$

Designating the 4×4 coefficient matrix in equation 33 as $\mathbf{P}$, the α values are determined by

$$\boldsymbol{\alpha} = \mathbf{P}^{-1}\boldsymbol{\gamma} \tag{34}$$

The tangential transverse shear strains, $\gamma^{(i)}$, can be related to the shear strains, γ_ξ and γ_η, by

$$\begin{bmatrix} \gamma^{(1)} \\ \gamma^{(2)} \\ \gamma^{(3)} \\ \gamma^{(4)} \end{bmatrix} = \begin{bmatrix} 1 & 0 & 0 & 0 & 0 & 0 & 0 & 0 \\ 0 & 0 & 0 & 1 & 0 & 0 & 0 & 0 \\ 0 & 0 & 0 & 0 & 1 & 0 & 0 & 0 \\ 0 & 0 & 0 & 0 & 0 & 0 & 0 & 1 \end{bmatrix} \begin{bmatrix} \gamma_\xi^{(1)} \\ \gamma_\eta^{(1)} \\ \gamma_\xi^{(2)} \\ \gamma_\eta^{(2)} \\ \gamma_\xi^{(3)} \\ \gamma_\eta^{(3)} \\ \gamma_\xi^{(4)} \\ \gamma_\eta^{(4)} \end{bmatrix} \tag{35}$$

If the 4×8 coefficient matrix in equation 35 is designated as $\mathbf{T}$, then the transverse shear strain field can be described in terms of values at the sampling points as

$$\begin{bmatrix} \gamma_\xi \\ \gamma_\eta \end{bmatrix} = \mathbf{A}\mathbf{P}^{-1}\mathbf{T} \begin{bmatrix} \gamma_\xi^{(1)} \\ \gamma_\eta^{(1)} \\ \gamma_\xi^{(2)} \\ \gamma_\eta^{(2)} \\ \gamma_\xi^{(3)} \\ \gamma_\eta^{(3)} \\ \gamma_\xi^{(4)} \\ \gamma_\eta^{(4)} \end{bmatrix} \tag{36}$$

Recall that, in element coordinates, $\boldsymbol{\gamma} = \mathbf{B}^{(s)}\mathbf{a}^{(e)}$, or in matrix form

$$\begin{bmatrix} \gamma_{xz}^{(1)} \\ \gamma_{yz}^{(1)} \\ \gamma_{xz}^{(2)} \\ \gamma_{yz}^{(2)} \\ \gamma_{xz}^{(3)} \\ \gamma_{yz}^{(3)} \\ \gamma_{xz}^{(4)} \\ \gamma_{yz}^{(4)} \end{bmatrix} = \begin{bmatrix} \mathbf{B}_1^{(s)} & \mathbf{B}_2^{(s)} & \mathbf{B}_3^{(s)} & \mathbf{B}_4^{(s)} \end{bmatrix} \begin{bmatrix} u_1 \\ v_1 \\ w_1 \\ \theta_{x1} \\ \theta_{y1} \\ . \\ . \\ . \\ u_4 \\ v_4 \\ w_4 \\ \theta_{x4} \\ \theta_{y4} \end{bmatrix} \tag{37}$$

The relationship between shear strain in natural and element coordinates is based on the Jacobian matrix (discussed in Section 2.4) and in this case written as

$$\begin{bmatrix} \gamma_{\xi}^{(1)} \\ \gamma_{\eta}^{(1)} \\ \gamma_{\xi}^{(2)} \\ \gamma_{\eta}^{(2)} \\ \gamma_{\xi}^{(3)} \\ \gamma_{\eta}^{(3)} \\ \gamma_{\xi}^{(4)} \\ \gamma_{\eta}^{(4)} \end{bmatrix} = \begin{bmatrix} [\mathbf{J}]_{2\times2} & [\mathbf{0}]_{2\times2} & [\mathbf{0}]_{2\times2} & [\mathbf{0}]_{2\times2} \\ & [\mathbf{J}]_{2\times2} & [\mathbf{0}]_{2\times2} & [\mathbf{0}]_{2\times2} \\ & & [\mathbf{J}]_{2\times2} & [\mathbf{0}]_{2\times2} \\ sym. & & & [\mathbf{J}]_{2\times2} \end{bmatrix} \begin{bmatrix} \gamma_{xz}^{(1)} \\ \gamma_{yz}^{(1)} \\ \gamma_{xz}^{(2)} \\ \gamma_{yz}^{(2)} \\ \gamma_{xz}^{(3)} \\ \gamma_{yz}^{(3)} \\ \gamma_{xz}^{(4)} \\ \gamma_{yz}^{(4)} \end{bmatrix} \tag{38}$$

Designating the enlarged Jacobian matrix in equation 38 as $\mathbf{C}$, the element shear strain based on the assumed linear distribution can be defined as

$$\begin{bmatrix} \gamma_{xz} \\ \gamma_{yz} \end{bmatrix} = \mathbf{J}^{-1} \begin{bmatrix} \gamma_{\xi} \\ \gamma_{\eta} \end{bmatrix} = \mathbf{J}^{-1}\mathbf{A}\mathbf{P}^{-1}\mathbf{T}\mathbf{C}\mathbf{B}^{(s)} \begin{bmatrix} u_1 \\ v_1 \\ w_1 \\ \theta_{x1} \\ \theta_{y1} \\ . \\ . \\ . \\ u_4 \\ v_4 \\ w_4 \\ \theta_{x4} \\ \theta_{y4} \end{bmatrix} \tag{39}$$

or, in a reduced form

$$\boldsymbol{\gamma} = \bar{\mathbf{B}}^{(s)}\mathbf{a}^{(e)} \tag{40}$$

where $\bar{\mathbf{B}}^{(s)}$ represents the modified shear strain-displacement matrix to be used in the stiffness matrix calculation, and is given by

$$\bar{\mathbf{B}}^{(s)} = \mathbf{J}^{-1}\mathbf{A}\mathbf{P}^{-1}\mathbf{T}\mathbf{C}\mathbf{B}^{(s)} \tag{41}$$

2.4 Stiffness Integration

Full integration is performed using Gaussian quadrature in the natural element coordinate system. Natural coordinates are used as convenient integration bounds of -1 and 1. Gauss point locations are shown in Figure 5 and placed such that weight factors are equal to 1.0. A counter-clockwise node numbering convention is used and also shown in Figure 5. The Jacobian matrix is used to relate derivatives with respect to natural coordinates to those with respect to element node. In defining the strain-displacement matrix, $\mathbf{B}$, it is necessary to evaluate shape function derivatives with respect to element coordinates x' and y'. In general these may be related to derivatives with respect to ξ and η as

$$\begin{bmatrix} \partial N_i/\partial\xi \\ \partial N_i/\partial\eta \end{bmatrix} = \mathbf{J} \begin{bmatrix} \partial N_i/\partial x' \\ \partial N_i/\partial y' \end{bmatrix} \tag{42}$$

Thus, if integration is performed using the natural coordinate system, the shape functions are defined using node locations in the natural coordinate system, and the associated derivatives with respect to x' and y' seen in equations 13-15 should be multiplied by the Jacobian inverse as

$$\begin{bmatrix} \partial N_i/\partial x' \\ \partial N_i/\partial y' \end{bmatrix} = \mathbf{J}^{-1} \begin{bmatrix} \partial N_i/\partial\xi \\ \partial N_i/\partial\eta \end{bmatrix} \tag{43}$$

where $\mathbf{J}^{-1}$ is given by

$$\mathbf{J}^{-1} = \frac{1}{det(\mathbf{J})} \begin{bmatrix} J_{22} & -J_{12} \\ -J_{21} & J_{11} \end{bmatrix} \tag{44}$$

For a four node planar element, such as a shell, the Jacobian matrix is defined as

$$\mathbf{J} = \frac{1}{4} \begin{bmatrix} -(1-\eta) & (1-\eta) & (1+\eta) & -(1+\eta) \\ -(1-\xi) & -(1+\xi) & (1+\xi) & (1-\xi) \end{bmatrix} \begin{bmatrix} x_1 & y_1 \\ x_2 & y_2 \\ x_3 & y_3 \\ x_4 & y_4 \end{bmatrix} \tag{45}$$

where x_i and y_i are global nodal coordinates. The stiffness matrix is calculated as shown in equation 1, but in the natural coordinate system and with the modified strain-displacement and material matrices derived in Sections 2.1-2.3 as

$$\mathbf{K}^{(e)} = \int_{-1}^{1}\int_{-1}^{1} \bar{\mathbf{B}}^T\mathbf{D}\bar{\mathbf{B}} det(\mathbf{J}) d\xi d\eta \tag{46}$$

Or using Gaussian quadrature,

$$\mathbf{K}^{(e)} = \sum_{i=1}^{2}\sum_{j=1}^{2} \bar{\mathbf{B}}(\xi_i, \eta_j)^T \mathbf{D} \bar{\mathbf{B}}(\xi_i, \eta_j) det(\mathbf{J}) W_i W_j \tag{47}$$

Using full integration, the weight terms, W_i and W_j, can be set equal to 1.0 if the following locations in the natural coordinate system are used for the four integration points: $\left(1/\sqrt{3}, 1/\sqrt{3}\right)$, $\left(-1/\sqrt{3}, 1/\sqrt{3}\right)$, $\left(-1/\sqrt{3}, -1/\sqrt{3}\right)$, and $\left(1/\sqrt{3}, -1/\sqrt{3}\right)$.

Finally, once the element stiffness matrix has been obtained, it should be transformed into the global coordinate system. This is necessary because the element DOF, θ_x and θ_y, when rotated in three-dimensional space, can result in a third rotational component θ_z that is not present in the element formulation. The stiffness matrix for the six DOF per node element for use in the global coordinate system is given by

$$\mathbf{K}^{(G)} = \mathbf{T}^{(e)T} \mathbf{K}^{(e)} \mathbf{T}^{(e)} \tag{48}$$

where $\mathbf{T}^{(e)}$ is an assembly of smaller transformation matrices, $\mathbf{L}^{(e)}$. These transformation matrices relate global and element DOF at each node, i, where $\mathbf{a}_i^{(G)} = \mathbf{L}^{(e)} \mathbf{a}_i$ and

$$\mathbf{L} = \begin{bmatrix} \mathrm{c}(x'x) & \mathrm{c}(x'y) & \mathrm{c}(x'z) & 0 & 0 & 0 \\ \mathrm{c}(y'x) & \mathrm{c}(y'y) & \mathrm{c}(y'z) & 0 & 0 & 0 \\ \mathrm{c}(z'x) & \mathrm{c}(z'y) & \mathrm{c}(z'z) & 0 & 0 & 0 \\ 0 & 0 & 0 & -\mathrm{c}(y'x) & -\mathrm{c}(y'y) & -\mathrm{c}(y'z) \\ 0 & 0 & 0 & -\mathrm{c}(x'x) & -\mathrm{c}(x'y) & -\mathrm{c}(x'z) \end{bmatrix} \tag{49}$$

In equation 49, "c" designates the cosine function. The cosine angle notation refers to the angle between the identified coordinate axes. For example, $\mathrm{c}(x'x)$ is equal to the cosine of the angle formed between the element x'-axis and the global x-axis. The transformation matrix for the entire element has dimensions of 20×24 and is given by

$$\mathbf{T}^{(e)} = \begin{bmatrix} [\mathbf{L}]_{5\times6} & \mathbf{0} & \mathbf{0} & \mathbf{0} \\ \mathbf{0} & [\mathbf{L}]_{5\times6} & \mathbf{0} & \mathbf{0} \\ \mathbf{0} & \mathbf{0} & [\mathbf{L}]_{5\times6} & \mathbf{0} \\ \mathbf{0} & \mathbf{0} & \mathbf{0} & [\mathbf{L}]_{5\times6} \end{bmatrix} \tag{50}$$

2.5 Floating Node Method

The enriched shell element uses the Floating Node Method (FNM) to enable discrete representation of damage in a mesh by splitting elements where delaminations form. The FNM is described at length in [68]. It can be summarized briefly as follows. Extra DOF, "floating nodes," associated initially with zero stiffness, are embedded in an element formulation with predefined connectivity. If a discontinuity forms (such as a delamination), the floating nodes can be activated and used to define subregions, Ω_A and Ω_B, within an element. The creation of subregions does not modify the original global nodal definitions or DOF connectivity. In a solution

procedure, DOF associated with floating nodes that are not used are condensed out and not included in the numerical solution of the model.

Figure 6 is an illustration of a shell element formulation enriched with the FNM where a maximum of two subregions, i.e., one delamination, can exist. This limit of one delamination is used to simplify the following explanation; however, the same approach can be used to accommodate multiple delaminations. Two states are shown, with and without the discontinuity. In the case where a delamination does not exist, the material integration is through the entire laminate thickness, $-h/2$ to $h/2$. In the case where a discontinuity does exist, the material integration in the z' direction is split into two parts, one for each subregion, at the z'-coordinate of the delamination, z_d. An element can be defined with as many floating nodes as desired if representation of more than one delamination is needed.

If an element is split into two or more subregions, each subregion stiffness matrix must undergo an offset transformation to account for the fact that the neutral axis of the subregion is offset from that of the original element definition. The offset causes coupling of membrane forces and nodal rotations in the subregion. This transformation is performed with an offset matrix and is given by

$$\mathbf{K}'_{\Omega_i} = \mathbf{T}^{(\text{off})T}\mathbf{K}_{\Omega_i}\mathbf{T}^{(\text{off})} \tag{51}$$

$\mathbf{T}^{(\text{off})}$ is the sum of a 24×24 identity matrix and off-diagonal terms given by

$$\begin{aligned}
T^{(\text{off})}_{1,5} &= -d \\
T^{(\text{off})}_{2,4} &= d \\
T^{(\text{off})}_{7,11} &= -d \\
T^{(\text{off})}_{8,10} &= d \\
T^{(\text{off})}_{13,17} &= -d \\
T^{(\text{off})}_{14,16} &= d \\
T^{(\text{off})}_{19,23} &= -d \\
T^{(\text{off})}_{20,22} &= d
\end{aligned} \tag{52}$$

where d is the offset distance between the neutral axis of a subregion and the original neutral axis of the element formulation.

3 Damage Simulation Algorithm

An algorithm combining the shell element formulation, the FNM, and VCCT was created to simulate damage growth in a laminate.

3.1 Delamination growth

The Virtual Crack Closure Technique (VCCT) is used with the enriched shell to predict delamination growth after convergence of each increment in an analysis

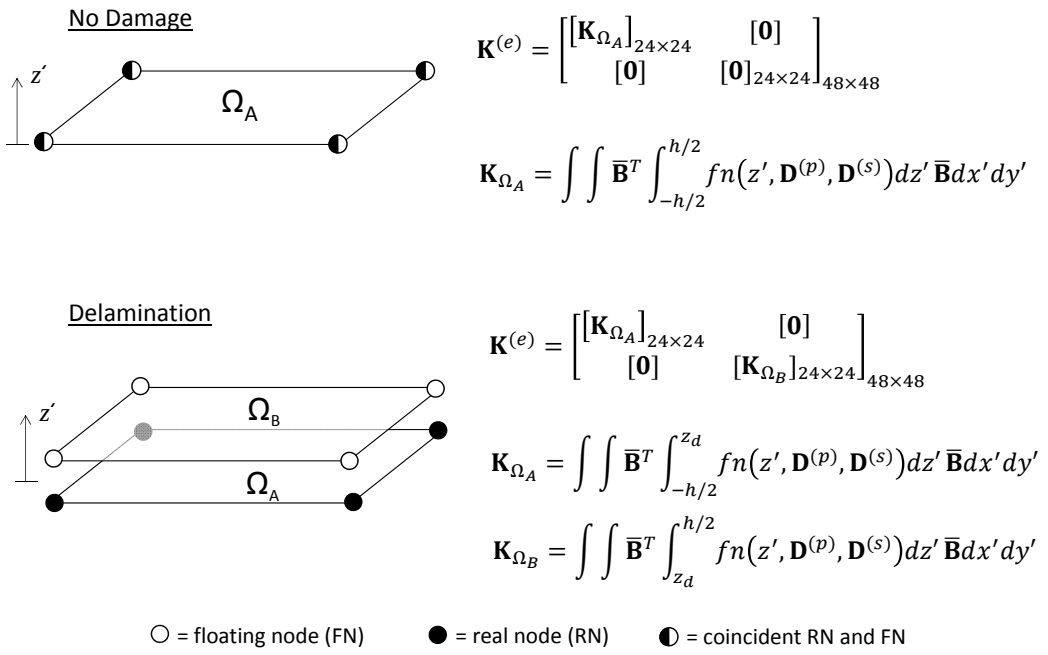

Figure 6. Floating Node Method.

solution procedure (similar to Orifici et al [48]). Subregions in split shell elements are tied together at nodes along a delamination front. At each tied node along a delamination front, energy release rate is calculated using the tie forces and the nodal displacements in the crack wake. This is illustrated in Figure 7 for a delamination front node (i, j). The prime superscript identifies "upper" nodes. Equations for calculating energy release rate when using shell elements were determined by Wang et al. [58]. These equations are given below using energy release rate calculation at delamination front node (i, j) in Figure 7 as an example

$$G_I = \frac{-1}{2\Delta A}\Big[F_z^{(i,j)}\Big(w^{(i-1,j)'} - w^{(i-1,j)}\Big) + M_x^{(i,j)}\Big(\theta_x^{(i-1,j)'} - \theta_x^{(i-1,j)}\Big) + M_y^{(i,j)}\Big(\theta_y^{(i-1,j)'} - \theta_y^{(i-1,j)}\Big)\Big] \tag{53}$$

.

$$G_{II} = \frac{-1}{2\Delta A}\Big[F_x^{(i,j)}\Big(u^{(i-1,j)'} - u^{(i-1,j)}\Big)\Big] \tag{54}$$

$$G_{III} = \frac{-1}{2\Delta A}\Big[F_y^{(i,j)}\Big(v^{(i-1,j)'} - v^{(i-1,j)}\Big) + M_z^{(i,j)}\Big(\theta_z^{(i-1,j)'} - \theta_z^{(i-1,j)}\Big)\Big] \tag{55}$$

where ΔA is the change in crack area if the nodal tie is released. The moment terms go to zero if rotational DOF are not included in the ties. For cases where the element size ahead of a crack tip is different than the element size in the wake, a correction factor must be applied to equations 53-55. Correction factors based on a $1/\sqrt{r}$ stress field singularity at the crack tip were derived by Rybicki and Kanninen [30]. If necessary, corrected values for energy release rate, designated by a prime superscript, can be obtained by

$$G'_I = G_I \sqrt{\frac{\Delta a_1}{\Delta a_2}} \tag{56}$$

$$G'_{II} = G_{II} \sqrt{\frac{\Delta a_1}{\Delta a_2}} \tag{57}$$

$$G'_{III} = G_{III} \sqrt{\frac{\Delta a_1}{\Delta a_2}} \tag{58}$$

where Δa_1 refers to element length in the crack wake and Δa_2 refers to element length ahead of the crack tip. The total energy release rate, G_T, is calculated by

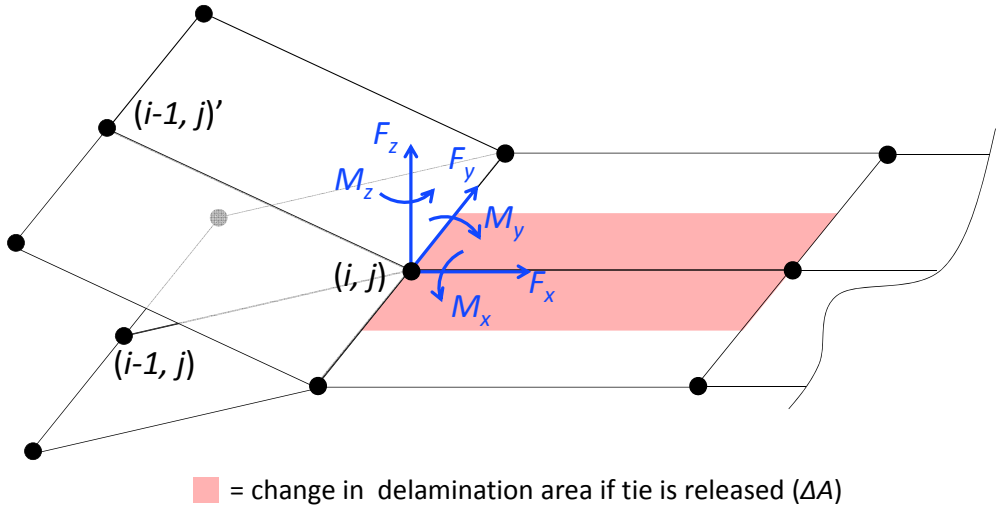

Figure 7. Virtual Crack Closure Technique tie forces and nodal displacements.

summing the modal components and is given by

$$G_T = G_I + G_{II} + G_{III} \tag{59}$$

The value for G_T is calculated at each delamination front node and compared to a critical value, G_c. If $G_T > G_c$, then delamination growth is predicted and that nodal tie is released. Mixed-mode G_c is calculated using the Benzeggah-Kenane equation [86]

$$G_c = G_{Ic} + (G_{IIc} - G_{Ic})(G_{II}/G_T)^{\eta_{BK}} \tag{60}$$

where G_{Ic} and G_{IIc} are critical energy release rate for Mode I and Mode II cracks, respectively, and η_{BK} is an experimentally determined parameter.

Specifically, for the enriched shell formulation, elements are split in the vicinity of a delamination front as shown in Figure 8. In an element formulation where a maximum of one delamination can exist (i.e., four real nodes and four floating nodes), there are four possible damage states for an element, as shown in Figure 8: (1) No damage - floating nodes are unused; (2) element is split - all floating nodes are tied to corresponding real nodes; (3) element is split - one or more node ties are released; and (4) element is split - all node ties released. Damage state (2) is used to represent one or more elements ahead of a delamination front.

As shown in Figure 8b, at a given delamination front node (i, j), G_T is calculated along mesh lines in four directions. The maximum G_T only is then used in the growth criterion. For delamination growth in non-physical or unlikely directions (such as $-x$ or $+/-y$ in Figure 8b), G_T is calculated as approximately zero due to the nodes in what would be the crack wake being tied together and, therefore, numerically, delamination growth is eliminated as a possibility. If an element has more than one delamination front (i.e., at different ply interfaces), this same procedure is performed for each one.

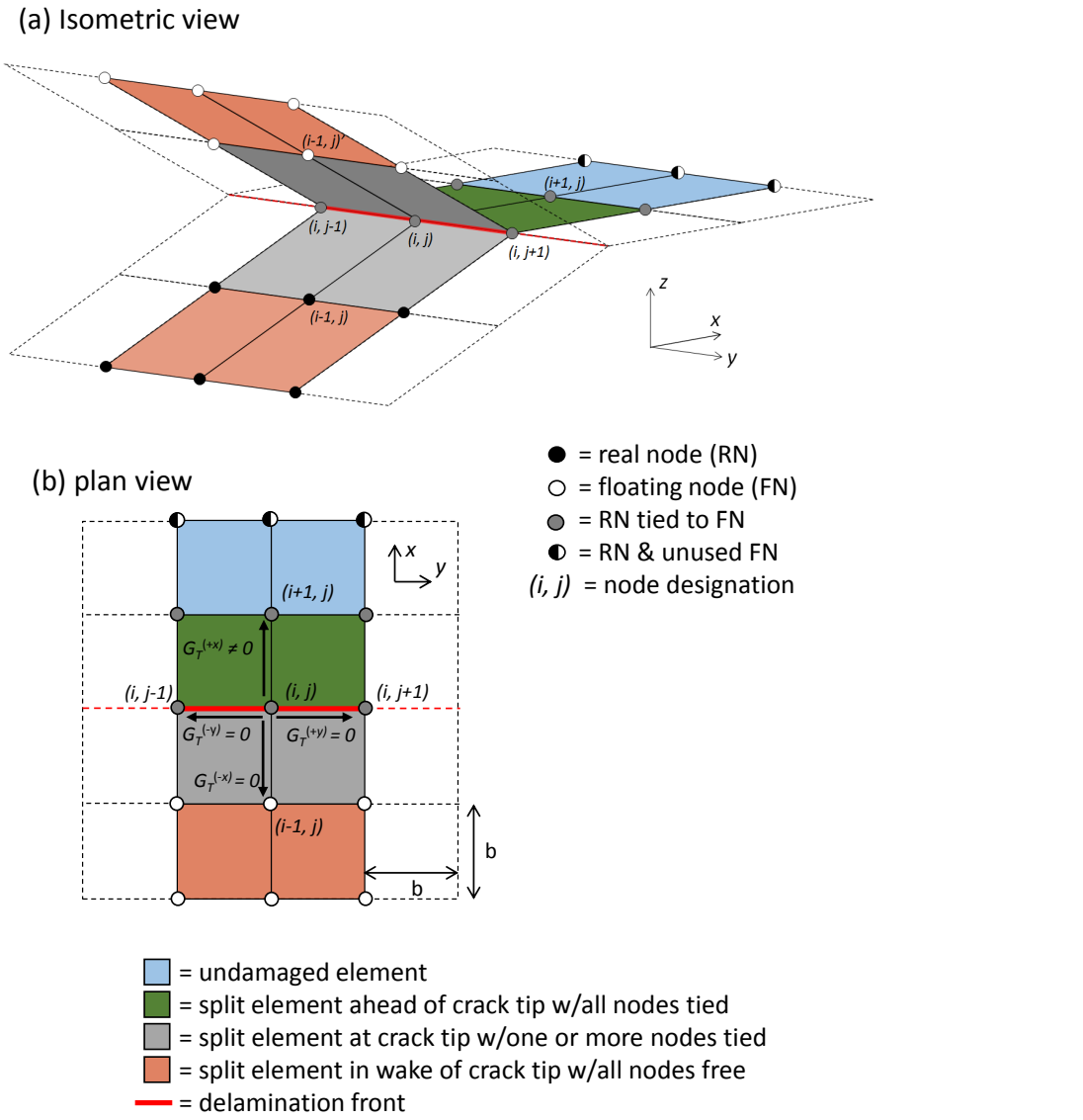

Figure 8. Element splitting in the vicinity of a delamination front.

3.2 Delamination-migration

3.2.1 Delamination-migration: representation

Figure 9a shows a computed tomography scan of a composite laminate test specimen where a delamination, after some initial growth, migrated through a ply via a transverse matrix crack to a different interface where its growth continued. An example model shown in Figure 9b illustrates how this type of damage feature is traditionally represented in a finite element mesh. When using shell elements, a different approach must be taken to represent out-of-plane damage features.

The physical schematic in Figure 10a shows a delamination-migration that has occurred in a cross-ply specimen (similar to the damage seen in Figure 9). Using

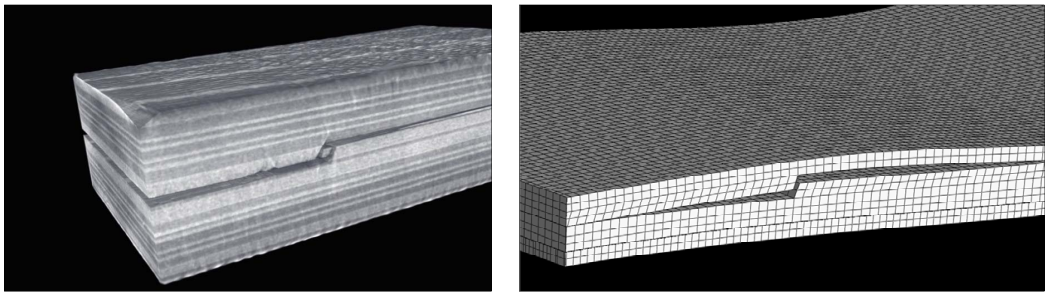

(a) Example of delamination migration in a laminate test specimen (computed tomography scan)

(b) Example of delamination-migration representation in a solid element mesh

Figure 9. Delamination migration in a test specimen and in a solid element mesh.

the physical schematic as a guide, Figure 10b shows how the transverse crack is represented in a shell mesh. The transverse matrix crack is not modeled explicitly as a discontinuity in the mesh, but rather the effect of the matrix crack is included in the model as a discontinuity in stiffness between elements. More specifically, in terms of the element formulation, there is a discontinuity from one element to another in the z' integration bounds in equations 22a-22d and in equation 27.

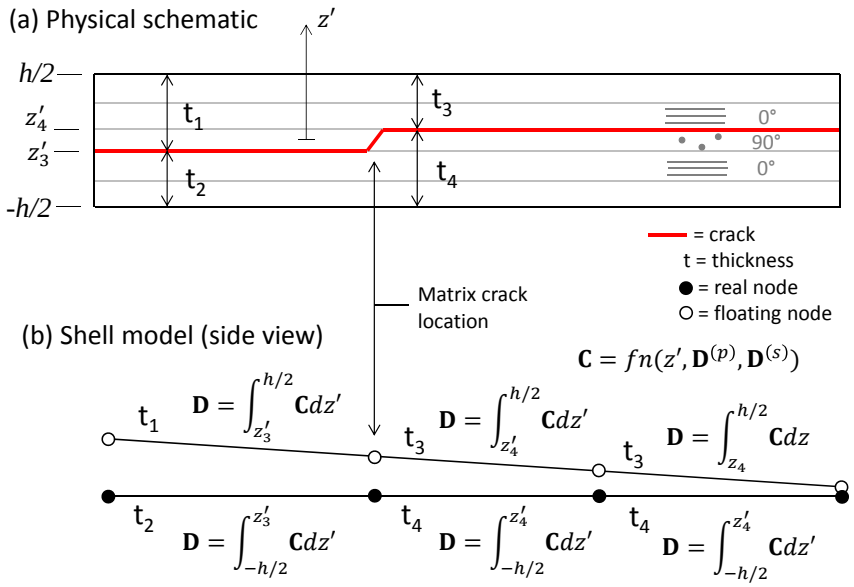

Figure 10. Representation of delamination migration in a shell mesh.

3.2.2 Delamination-migration: prediction

A straightforward two-step criterion similar to that used by De Carvalho [47] is used to predict delamination-migration. O'Brien observed that many Mode I microcracks form ahead of a shear delamination front in the resin-rich region at the ply interface where the delamination is located [87]. The first step of the delamination-migration prediction is based on determining the orientation of these microcracks [77]. If the microcracks are pointed towards and reach fibers that have an orientation that arrests their growth, they will coalesce into a macrocrack, be redirected along the bounding fiber direction, and can be observed as a delamination. If the microcracks are not contained by bounding fibers, they still may coalesce, but instead of forming a delamination, they form a transverse matrix crack that grows in between fibers though a ply (i.e., migration). Therefore, if the microcrack orientation is known, and given the adjacent bounding fiber orientation, the possibility of migration can be determined.

In an experiment developed by Ratcliffe et al., the microcrack orientation and subsequent tendency for delamination kinking (i.e., migration) was found to be a result of the sign of the shear stress at the delamination front [75]. This concept is illustrated in Figures 11a and 11b where a hypothetical small stress element is shown at a delamination tip under two possible shear deformation states. The two states are shown in Figure 11b as deformed elements with a Mode I microcrack whose orientation is a result of the sign of the shear stress. The shear sign and the direction of delamination propagation are the only pieces of information needed to indicate whether the microcracks are pointed at the fibers above the delamination or pointed at the fibers below the delamination. The shear sign is obtained from the tie forces at nodes in the enriched shell element model as described previously. This is illustrated in Figure 11c.

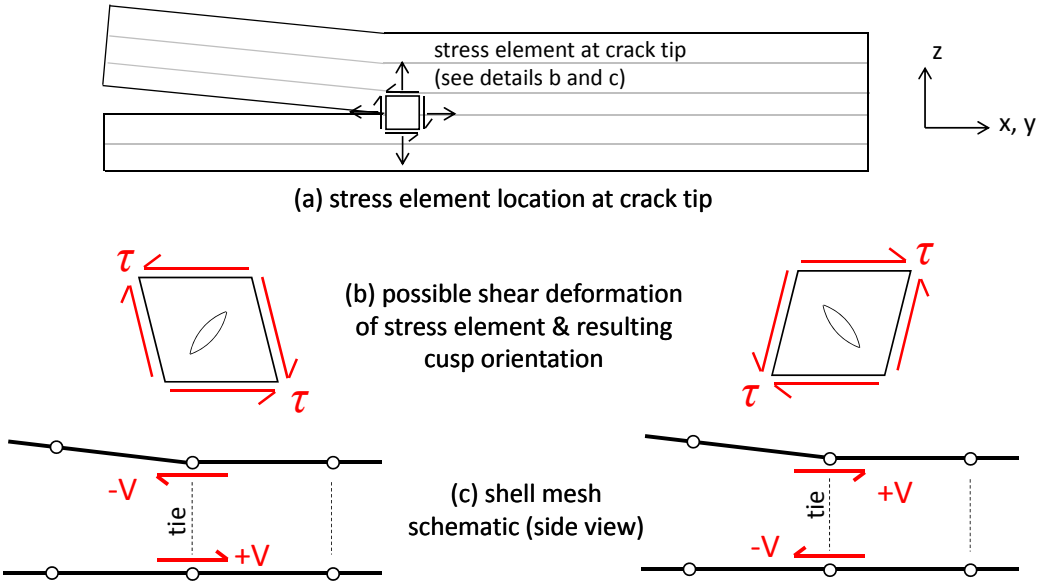

Figure 11. Delamination-migration prediction - Step 1: Shear sign.

The second step in predicting delamination-migration consists of an energy based criterion. In the enriched shell model, formation of a transverse matrix crack, as in migration, only occurs if that crack is associated with a delamination advance. A tied delamination front node has three options within the damage algorithm when it is evaluated in between converged solution increments: (1) No damage - tie remains in place , (2) Delamination without migration - tie is released and elements in the direction of propagation are split at the current interface, or (3) delamination and migration - the tie is released and elements in direction of propagation are split at a new interface. This is summarized in Figure 12 which shows the energy criterion for each option. In Figure 12, G_c refers to the toughness for delamination and $G_c^{(tr)}$ refers to the toughness of a transverse crack.

Some things to note regarding the energy criteria shown in Figure 12 are (1) the fracture toughness to cause breaking fibers is assumed to be infinite (i.e., no fiber failure in the current implementation), (2) an assumption is made that the transverse matrix cracks are small and insignificant in terms of energy dissipated when compared to delaminations [88], (3) G_T at the current crack tip location is assumed to be approximately unchanged after the formation of a transverse matrix crack leading to the next interface (i.e., after migration), and (4) G_T calculated using VCCT as described previously to predict delamination growth is also used to predict transverse matrix crack growth originating from the same location [47].

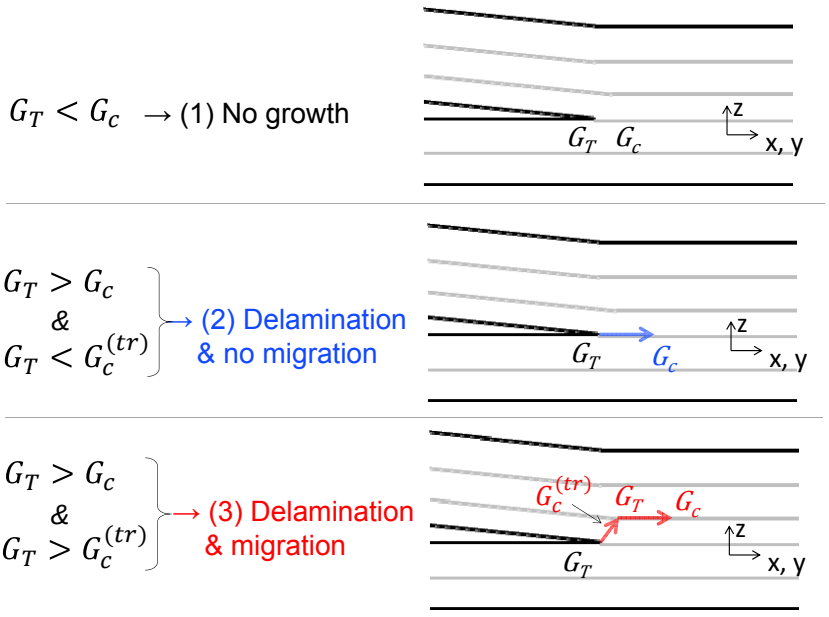

Figure 12. Delamination-migration prediction - Step 2: Energy criteria.

4 Element Verification and Validation

Numerical benchmark and experimental data were used to verify and validate the enriched shell element and to study the accuracy of the assumptions made for the VCCT implementation. Double Cantilever Beam (DCB), End Notch Flexure (ENF), Mixed Mode Bending (MMB), and Single Leg Bending (SLB), were considered as numerical benchmark cases for verification [89]. Benchmark data corresponding to displacement controlled tests are shown and compared to the shell model results. A previous delamination-migration experiment was used for experimental validation [47]. All analyses were static with linear ramped loads and run in Abaqus 6.14/Standard®. The enriched shell element and damage algorithm were coded in user defined element and external database subroutines, respectively. Material properties used in each of the models are given by Table 1 [89].

Table 1. Numerical benchmark material and strength properties (all unidirectional graphite/epoxy prepreg) [89].

Property	DCB	ENF, MMB, DM*	SLB	Units
Material	T300/1076	IM7/8552	C12K/R6376	
E_{11}	139.4	161	146.9	GPa
$E_{22} = E_{33}$	10.16	11.38	10.6	GPa
$G_{12} = G_{13}$	4.6	5.2	5.45	GPa
G_{23}	3.54	3.9	3.99	GPa
$\nu_{12} = \nu_{13}$	0.3	0.32	0.33	-
ν_{23}	0.43	0.45	0.33	-
G_{Ic}	0.17	0.212	0.341	kJ/m^2
G_{IIc}	0.494	0.774	1.286	kJ/m^2
η_{BK}	1.62	2.1	3.39	-

* DM = delamination-migration

4.1 Numerical Verification

A description of each model is given in the following sections. Because the models consist of initially planar coincident shell elements, they are shown in a deformed state to better illustrate their features. Multiple mesh sizes were considered in each case as summarized in Table 2. By considering multiple mesh sizes, the ratio $\Delta a/h'$ was effectively varied where Δa is crack extension length and h' is element thickness or the thickness of one region of a split element. This aspect ratio is relevant both in the context of damage simulation and linear elastic accuracy as shell elements may not perform well when the element edge dimension is significantly less than the thickness. Generally, all analyses were run with a solution step length of 1.0 and a constant increment size of 0.002.

Table 2. Summary of mesh sizes considered in verification models (units in mm, $\Delta a/h'$ corresponds to a subregion in a damaged element).

	Mesh 1		Mesh 2		Mesh 3	
Model	Size	$\Delta a/h'$	Size	$\Delta a/h'$	Size	$\Delta a/h'$
DCB	1.0	0.66	2.5	1.66	5.0	3.30
ENF	1.0	0.44	2.5	1.11	5.0	2.22
MMB	1.0	0.44	2.5	1.11	5.0	2.22
SLB	1.0	0.49	2.0	0.98	5.0	2.46

4.1.1 Double Cantilever Beam

Numerical benchmark data from Krueger [89] were used to verify the enriched shell element's accuracy in simulating a pure Mode I delamination. A schematic of the DCB test specimen and an overview of the finite element model are shown in Figure 13.

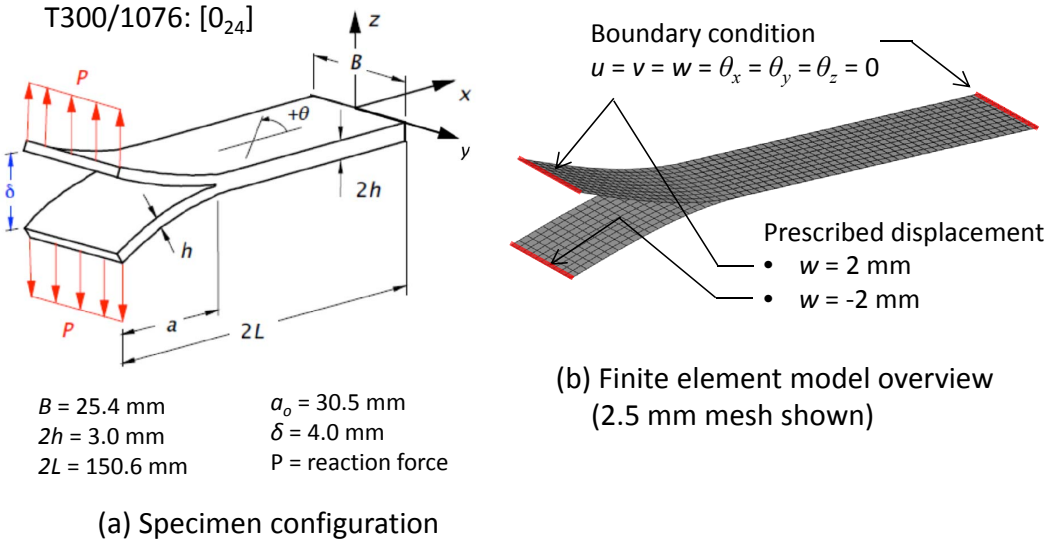

Figure 13. DCB specimen and model description.

When modeling a double cantilever beam (DCB) specimen, the constrained DOF in the ties at the delamination front and the number of elements in damage state 2 (i.e., split but still tied) ahead of the delamination front both affect the response. Three cases, as summarized in Table 3, are used to demonstrate and justify the preferred mesh and tie configuration. The number of split elements ahead of the delamination front is maintained as the front advances in the simulations.

Due to the symmetric nature of the DCB specimen configuration and loading,

Table 3. Summary of three DCB cases with varying delamination front tied DOF and number of elements split but tied ahead of the delamination.

Case	DOF tied	Number of elements split ahead of crack tip
1	$u, v, w, \theta_x, \theta_y$	1
2	u, v, w	1
3	u, v, w	7, mesh = 1.0 mm 4, mesh = 2.5 mm 2, mesh = 5.0 mm

each bending arm can be thought of as a cantilever beam supported at the crack tip with a point load at the end. The boundary condition at the crack tip is somewhat complex as the material supporting the bending arms ahead of the crack tip can deform in the axial direction and effectively allow a small amount of rotation. This root rotation would be captured in a high fidelity model where the specimen is meshed through the thickness with multiple elements; however, this level of mesh fidelity is not present in a beam or shell model. Cotterell et al. proposed a method to simulate a small amount of root rotation in a simple beam model by increasing total crack length (i.e. increasing flexibility) [90]; however, it is not clear if this type of approach is viable in a general three-dimensional FE model. This type of approach was not investigated in detail for the enriched shell.

The three cases described in Table 3 were investigated in an attempt to determine an accurate means to include the effects of root rotation in the structural stiffness of the specimen. Case 1 has rotations constrained in the ties at the delamination front and, therefore, does not account for any root rotation. Case 2 is considered as a means to relax the boundary condition present in case 1 and allow some form of root rotation by releasing rotations in the nodal ties. Case 3, also with rotations in the ties released, provides a more relaxed boundary condition compared to case 1 but more stiffness when compared to case 2 by splitting more than one element ahead of the crack tip. A diagram of the case 3 mesh is shown in Figure 14, where multiple elements are split ahead of the delamination front along the axis $\hat{x}$ up to a distance of $\hat{x}_{max}$.

DCB force-displacement correlations are shown in Figure 15 for cases 1-3 as described in Table 3. In all cases, the sawtooth behavior seen in the force-displacement curves can be explained by the sudden release of a tied crack tip node as the delamination advances one element length. This behavior is seen to diminish with mesh refinement. In case 1, the good agreement of the critical force magnitude seen in Figure 15a, shows that the energy release rate appears to be predicted well; however, the stiffness of the model prior to damage is over predicted by approximately 24%. Also of note in the case 1 results is that stiffness and energy release rate prediction are not affected by mesh size. Case 2 does not constrain rotations in the ties and splits one element ahead of the delamination. It is clear from Figure 15b that it is

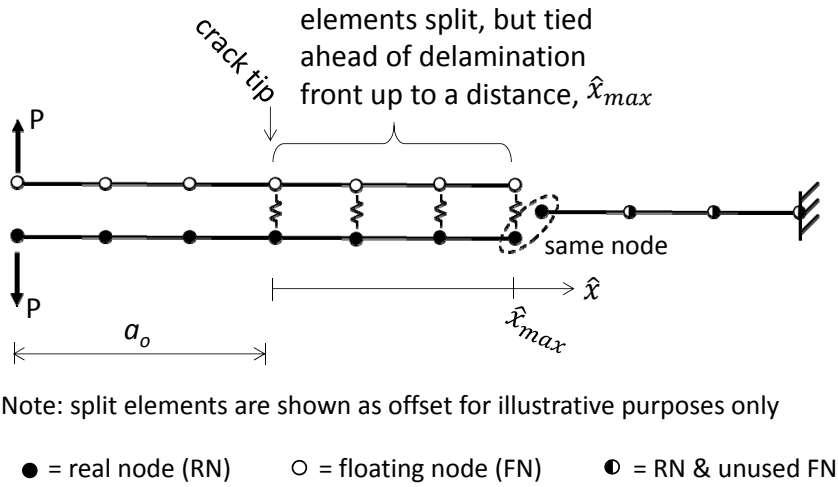

Figure 14. Diagram of mesh for case 3: rotations are unconstrained in split element ties and multiple elements ahead of the delamination are split and tied together.

possible to match the stiffness well with this approach; however, both the stiffness and energy release rate are mesh dependent.

Results from the case 3 configuration, where tie rotations are unconstrained and more than one element ahead of the delamination is split, are shown in Figure 15c. Case 3 was found to produce accurate stiffness and energy release rate results and remove the mesh dependency seen in case 2. Although the size of the sawtooth spikes in the force-displacement curves do vary between meshes, the model stiffness and overall damage growth behavior are consistent for all meshes in case 3. The applied force at a given displacement for case 3 generally is under-predicted by less than 5% for all mesh sizes.

The effects of the different mesh configurations seen in Figures 15a and 15b may be explained using a beam analogy. Case 1 and case 2 are compared in Figure 16 using two beam models representative of the upper DCB bending arm in each case. By summing forces and moments and comparing analytical beam deflection formulae, it is shown that in case 2, the tie forces located at the crack tip and beam deflections to be used in VCCT calculations are a function of mesh size, b.

A closer examination of the case 3 model behavior is helpful to understand its functionality in more detail. A version of the case 3 model for each mesh size was created in which all elements up to 15 mm away from the delamination front were split and tied together (i.e., $\hat{x}_{max} = 15.0$ mm). Accordingly, 15, 6, and 3 elements are split ahead of the delamination front in the 1.0 mm, 2.5 mm, and 5.0 mm mesh models, respectively. Using these modified case 3 models, the force, F_z, in each of the nodal ties in the split elements is normalized by the value at the crack tip and plotted versus $\hat{x}$ in Figure 17b. The definitions for $\hat{x}$ and $\hat{x}_{max}$ are shown again in Figure 17a for convenience. Figure 17b shows that the applied DCB load is not carried entirely by one or two ties in the vicinity of the crack tip, as case 2

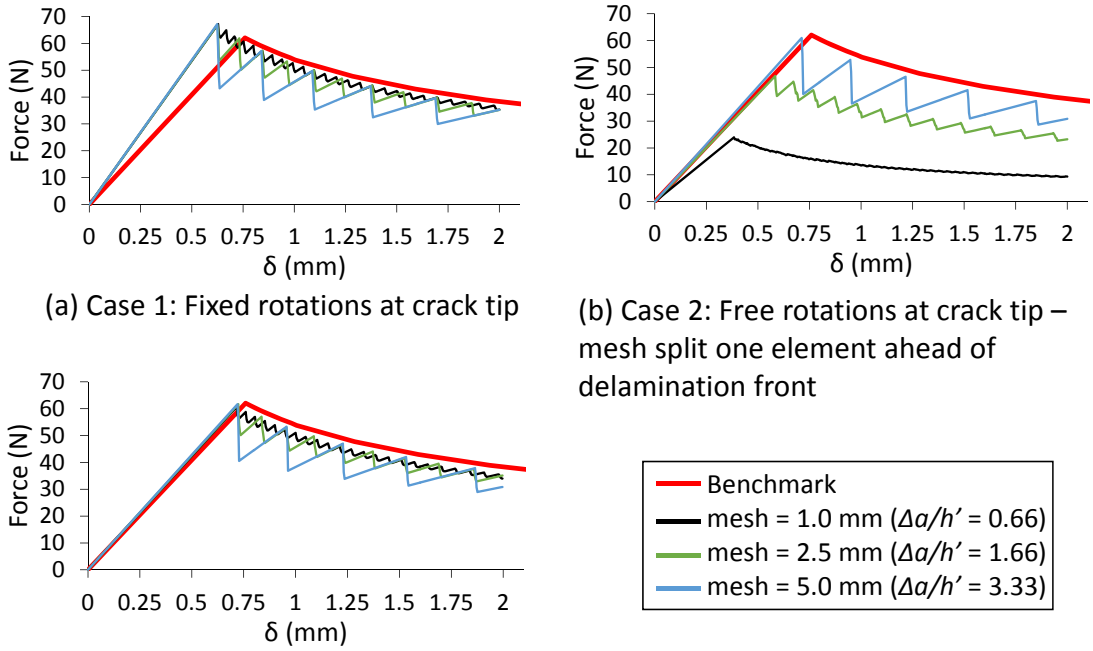

Figure 15. DCB: Force-displacement correlation.

effectively assumes, but by as many nodes as are present in a fixed distance ahead of the delamination front.

The tie force in all mesh sizes is seen in Figure 17b to converge to zero at approximately $\hat{x} = 10.0$ mm, indicating that in this particular DCB specimen, all nodes within the range of $0 \leq \hat{x} \leq 10.0$ mm help to resist the applied load. Intuitively then, if there are no ties present within the 10.0 mm range or up until the force has sufficiently vanished, the applied load is resisted globally by what amounts to an inaccurate boundary condition for the DCB bending arms. This is what happens in case 2, where there is only one node resisting the applied load ahead of the delamination. Figure 17b also illustrates why the 5.0 mm mesh is the most accurate within case 2 as the single supporting node ahead of the delamination is located farther along the curve closer to the point where the tie loads vanish. A generally applicable method has not yet been determined to calculate critical element length (i.e., maximum mesh size) and how far ahead of a delamination the elements must be split.

Figure 17c complements the previous conclusions made using Figure 17b. Energy release rate convergence for each case 3 mesh is plotted versus $\hat{x}_{max}$. Note that the first data point for each curve in this plot is equivalent to case 2. In all curves, energy release rate is obtained from a node halfway across the specimen width at

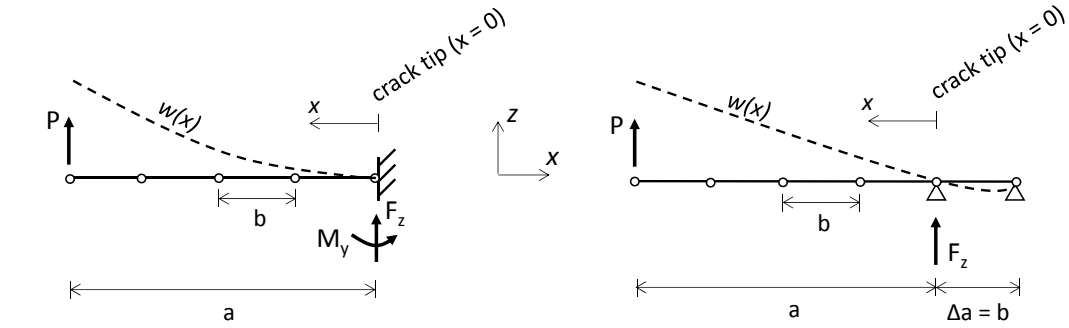

$\Sigma F_z = 0$: $F_z = -P$ $\quad \Sigma M_{x_o} = 0$: $M_y = Pa$

$$w(x) = \frac{P}{6EI}(2a^3 - 3a^2x + x^3)$$

VCCT forces, F_z & M_y, and deflection, $w(x)$, are NOT functions of mesh size, b

(a) rotations fixed at crack tip (Case 1)

$\Sigma M_{x_o} = 0$: $F_z = -P(a+b)/b$

$$w(x) = \frac{Px}{6EI}(2ab + 3ax - x^2)$$

VCCT force, F_z, and deflection, $w(x)$, are functions of mesh size, b

(b) rotations free at crack tip (Case 2)

Figure 16. Effect of constrained DOF at crack tip on VCCT forces and displacements for case 1 and case 2.

a common, but arbitrary, load step, prior to any damage initiation. Energy release rate predicted by all meshes converges to the same value, which also matches an analytical solution [91] given by

$$G_I = \frac{P^2 a^2}{BEI} \tag{61}$$

where P is the applied load, a is the initial crack length, B is the specimen width, E is the stiffness modulus set equal to E_{11} here, and I is the area moment of inertia.

Because of the observed accuracy in stiffness and energy release rate prediction and the overall mesh independence, the remaining results in this paper for all models are from the case 3 configuration with elements split up to 12 mm ahead of the delamination front. A nonlocal approach is used where a database in the form of a common memory block in the subroutine stores and updates the damage state of all elements in the model. This database may be modified after each converged solution increment to reflect additional damage growth.

Figure 18 is a plot of energy release rate in the DCB model across the delamination front, normalized by G_c. The data shown correspond to the load increment just before the first instance of damage growth. Results from each mesh size are included, along with an analytical solution given by equation 61. Although some small variance can be seen, the energy release rate does not exhibit an appreciable amount of mesh dependence over most of the specimen width for the mesh sizes con-

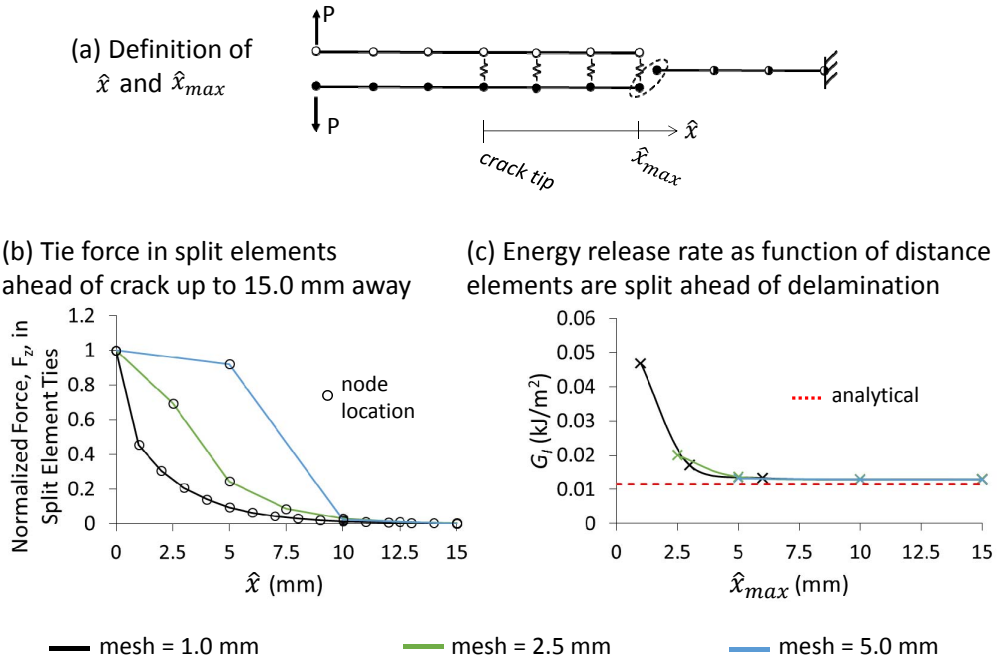

Figure 17. DCB: Tie forces in split elements ahead of crack tip and G_I as a function of distance elements are split ahead of the delamination.

sidered, except at the edges where the resolution in the finer meshes allows the drop in G to be represented in more detail. The average G_I from the 1.0 mm mesh model has an error of approximately 5% when compared to the analytical solution. This amount of error agrees with a similar observation made in the force-displacement curves in Figure 15c. Based on Figure 15c and Figure 18, meshes using the case 3 conditions, sized corresponding to a $\Delta a/h'$ ratio range of 0.66-3.33, where Δa is the mesh size and h' is half of the total laminate thickness, can produce accurate energy release rates using the enriched element for Mode I delaminations.

In Figure 19a, the DCB model with a 1.0 mm mesh is shown in plan view (i.e., looking in the negative z-direction) at the end of a load increment identified as "Frame 1" just prior to the load step where G_T exceeds G_c for the first time. Following Frame 1, sequential load increments (Frames 2-5 seen in Figures 19b-19e) demonstrate the process for the delamination to advance one row of elements with ties at nodes across the delamination front being released according to their energy release rate exceeding G_c, as shown in the plots of G_T for each frame. This process repeats one row at a time throughout propagation.

This manner of delamination advancement through the mesh is not physically accurate, as typically delaminations in a DCB specimen form a curved front that advances at the same rate across the width of the specimen; however, it is equivalent to the behavior seen in three-dimensional high fidelity models [89]. The large spikes in energy release rate located at corner nodes on the delamination front do not

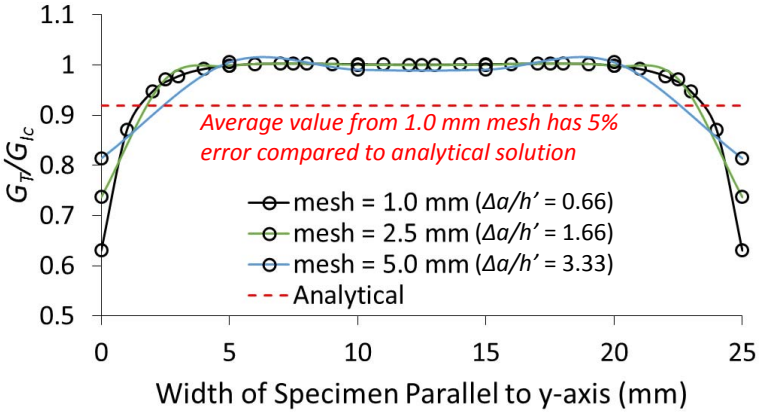

Figure 18. DCB: Results from mesh convergence study for normalized energy release rate, G_T/G_{Ic}, distribution across delamination front ($a = a_o = 30.5$ mm).

appear to cause any inaccuracies in the simulation of this specimen. The energy release rate spikes may be problematic in other analyses if there are more of them across the delamination front. For example, if a delamination front has a spike in G_T at every other node, it is reasonable to expect that delamination front to propagate too quickly. Work is ongoing to address any inaccuracies caused by energy release rate spikes in the enriched shell element.

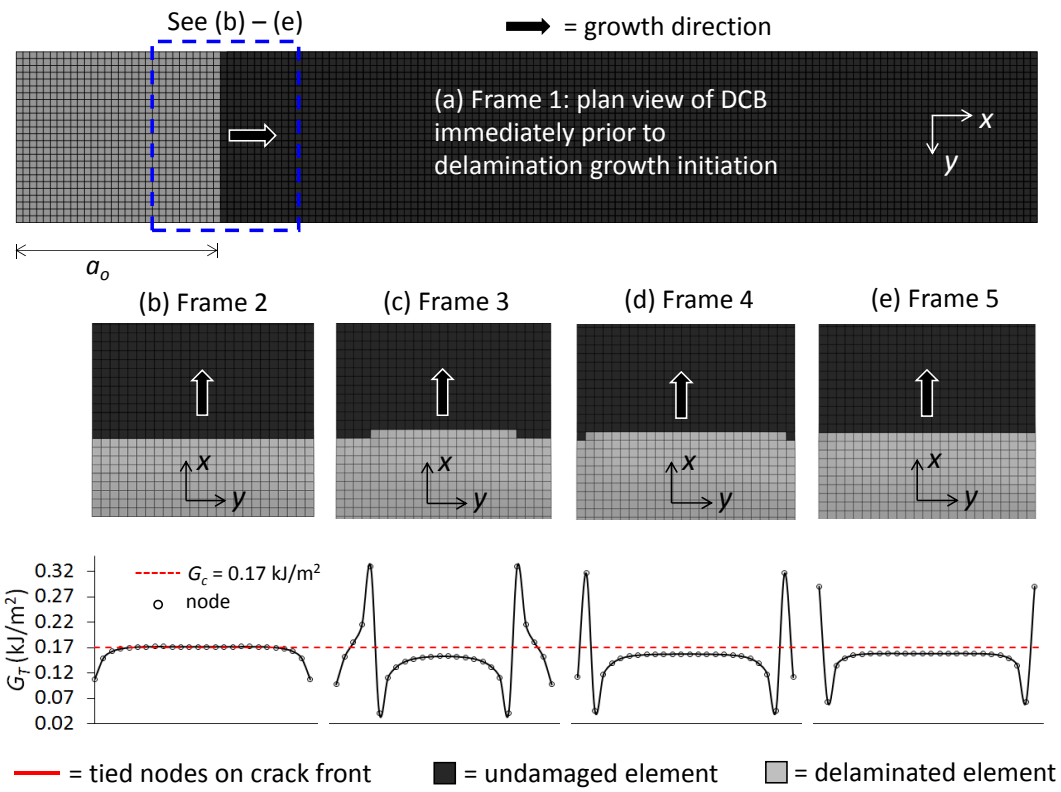

Figure 19. DCB: Delamination front geometry and energy release rate at the first instance of crack growth ($a = a_o = 30.5$ mm).

4.1.2 End Notch Flexure

Numerical benchmark data from Krueger [89] were used to verify the enriched shell element's accuracy in simulating a pure Mode II delamination. A schematic of the ENF test specimen and an overview of the finite element model are shown in Figure 20. In the ENF test, there exists a sliding contact interaction between the upper and lower regions of the specimen. Contact was simulated in the enriched element by tying real and floating nodes from each split region in the z'-direction.

Of interest in the ENF models is whether this rudimentary contact simulation method consisting of tying nodes in the z'-direction is accurate, as compared to a surface-based technique. Use of nodal ties is more computationally efficient and less prone to solution divergence than the surface based contact simulation and, therefore, is the preferred approach. Shown in Figure 21 are force-displacement data from the 2.5 mm mesh model using the Abaqus 6.14/Standard® surface-to-surface contact method and using the nodal tie approach. There is no appreciable difference in results between these two contact methods in these simulations. Therefore, the nodal tie technique was adopted for this study.

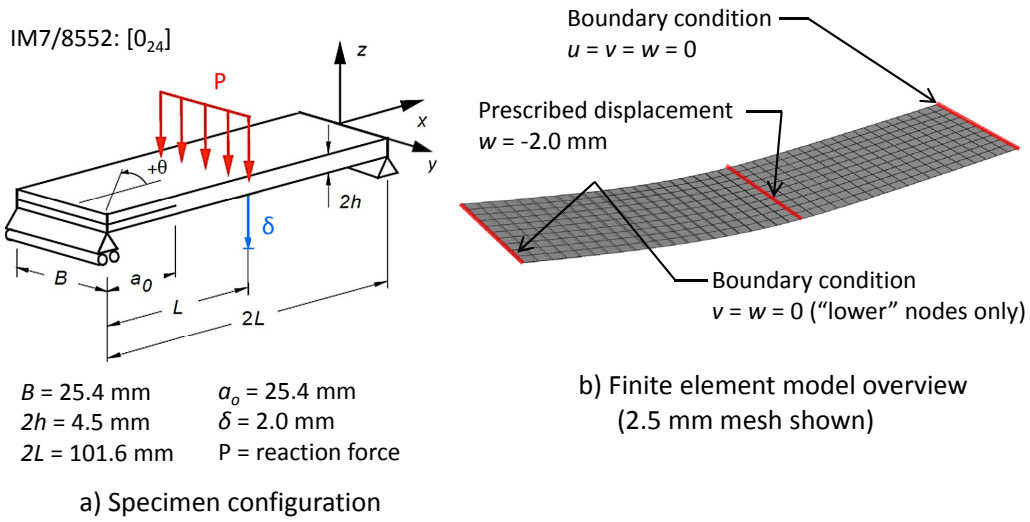

Figure 20. ENF specimen and model description.

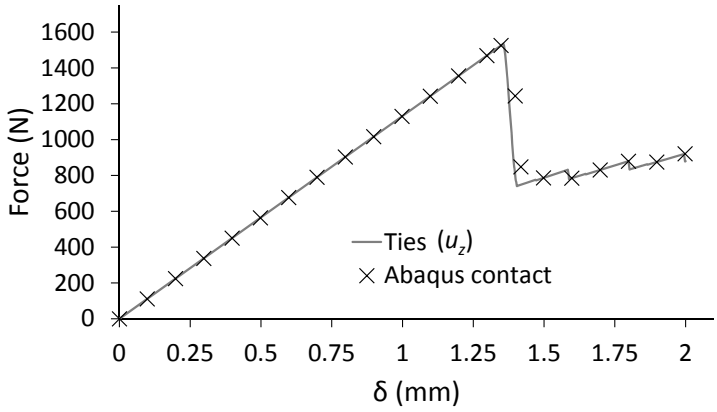

Figure 21. ENF: Force-displacement data comparing nodal tie and surface based contact simulation techniques.

Force-displacement data correlation for the ENF specimen is shown in Figure 22. The close match of the critical load and displacement indicates that Mode II energy release rate is well predicted by the enriched shell element. When the critical load is reached and damage initiates, unstable crack growth occurs and is characterized by a sudden drop in force in the enriched shell models that begins and ends in agreement with the benchmark. After the sudden load drop, the delamination growth eventually becomes stable and the “sawtooth” behavior is again seen aligning with the benchmark data and also diminishing with mesh refinement.

In the benchmark dataset, the critical force-displacement curve is also shown as a dashed line and appears where unstable growth occurs as decreasing displacement.

Krueger obtained the benchmark data by using multiple finite element models with varying initial crack lengths to predict the critical force and displacement at delamination onset. While the critical force data are useful as a robust means to create the benchmark data in regions of *stable* growth, the data do not represent actual physical behavior during the *instability* since a displacement controlled test could not experience negative displacement.

In Figure 23, the energy release rate distribution across the delamination front (normalized by G_c) is shown corresponding to a load prior to delamination growth initiation. The energy release rate magnitude and distribution shape do not vary with mesh size, with the exception of values at the specimen edges. This can be explained simply by the fact that the distance across which the energy release rate spikes near the edge is smaller than or similar to the element size in the coarser meshes and, therefore, the resolution is insufficient to characterize this feature. The localized differences in energy release rate seen in Figure 23, however, do not seem to cause a difference globally in specimen delamination growth as evidenced by the close alignment of models in the force-displacement plot shown in Figure 22. Based on Figures 22 and 23, a mesh size corresponding to a $\Delta a/h'$ ratio range of 0.44-2.22 can produce accurate energy release rates in the enriched element for Mode II delaminations.

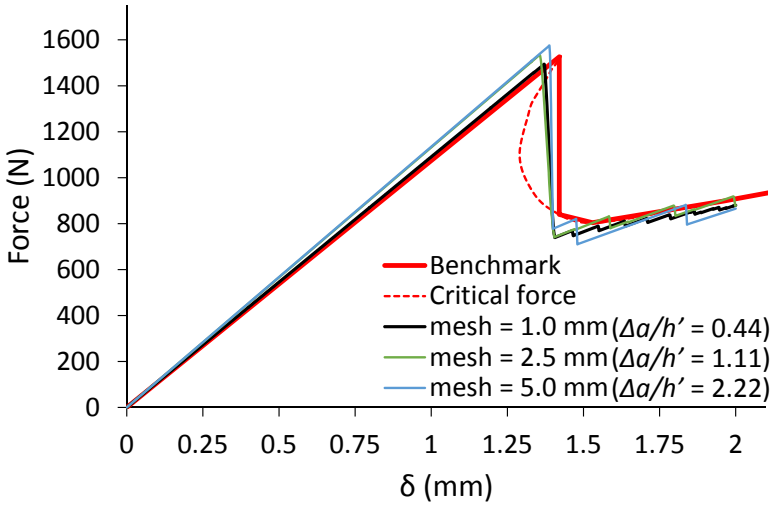

Figure 22. ENF: Force-displacement data correlation.

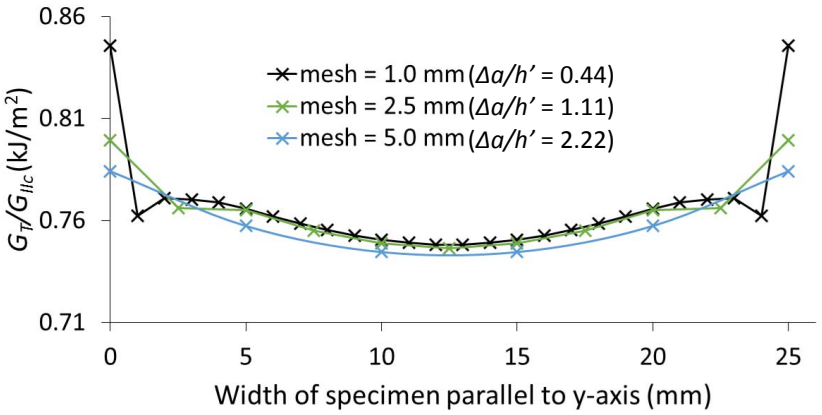

Figure 23. ENF: Results from mesh convergence study for normalized energy release rate, G_T/G_{IIc}, distribution across delamination front ($a = a_o = 25.4$ mm).

4.1.3 Mixed-Mode Bending

Numerical benchmark data from Krueger [89] were used to verify the enriched shell element's accuracy in simulating a mixed-mode delamination where $G_{II}/G_T = 0.8$. Three mesh sizes were considered: 1.0 mm, 2.5 mm, and 5.0 mm, which correspond to $\Delta a/h'$ ratios of 0.44, 1.11, and 2.22, respectively, in the damaged elements. A schematic of the MMB test specimen and an overview of the finite element model are shown in Figure 24. The loading apparatus was modeled using rigid elements (RB3D2).

Force-displacement correlation for the MMB is shown in Figure 25. The good agreement for critical load and displacement indicates that energy release rate and mode mixity are well predicted in the enriched element. The same type of unstable growth followed by the sawtooth force behavior, as discussed previously for the ENF, is seen here. Based on Figure 25, a mesh size corresponding to a $\Delta a/h'$ ratio range of 0.44-2.22 can produce energy release rates in the enriched element for mixed-mode delaminations when $G_{II}/G_T = 0.8$.

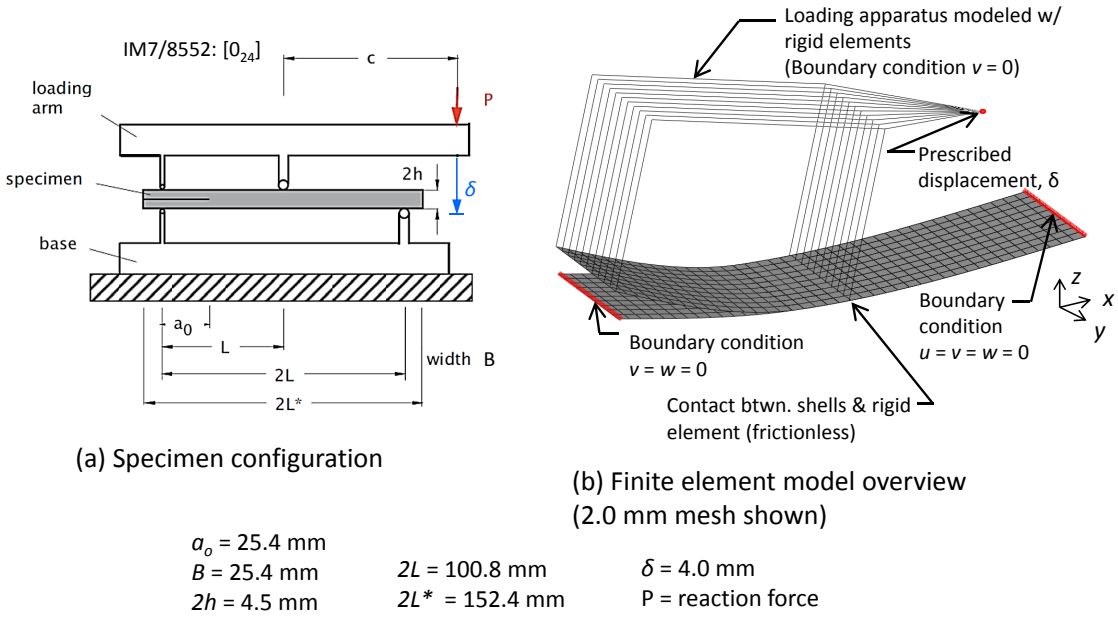

Figure 24. MMB specimen and model description.

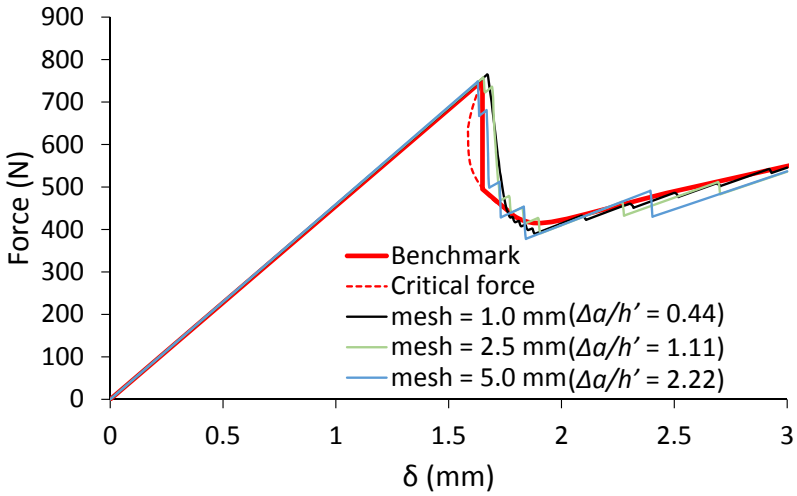

Figure 25. MMB: Force-displacement data correlation, $G_{II}/G_T = 0.8$.

4.1.4 Single Leg Bending

Numerical benchmark data from Krueger [89] were used to verify the enriched shell element's accuracy in simulating mixed-mode delamination where $G_{II}/G_T = 0.4$.

A schematic of the SLB test specimen and an overview of the finite element model are shown in Figure 26.

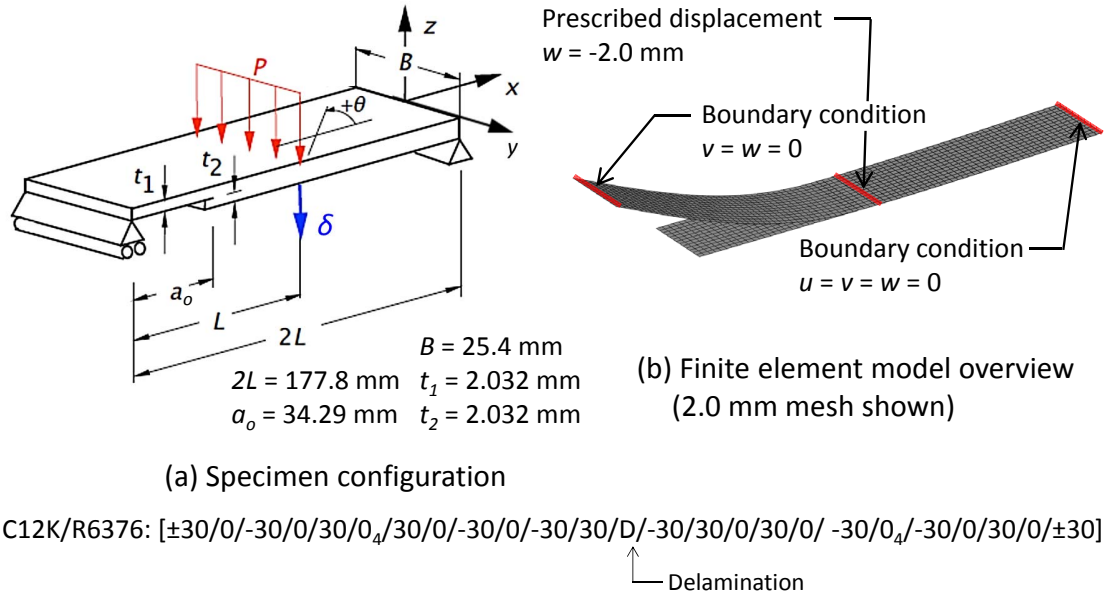

Figure 26. SLB specimen and model description.

Force-displacement correlation for the SLB is shown in Figure 27. The good agreement of the shell model results for critical force and displacement with the benchmark data indicates that energy release rate is well predicted in the enriched element. As in the ENF and MMB models, unstable growth is captured in the enriched element models by a rapid load drop that begins at the critical load and ends when the delamination growth becomes stable.

Of note in the SLB specimen is that the delamination is located at a +30/-30 interface. Past work has shown that when using VCCT in cases where elements on either side of a crack differ greatly in stiffness, mixed-mode energy release rate components may oscillate near the crack tip and not be calculated correctly [61], thereby introducing a mesh dependence. This phenomenon has primarily been investigated in high fidelity models where the elements adjacent to the bimaterial interface are representative of, and therefore, defined, based on the stiffness of a single ply. In the case of a shell element model, the adjacent elements are representative of the *laminate* on either side of the delamination and, therefore, could be similar in stiffness even though the two adjacent *lamina* on either side of the delamination may have varying stiffnesses (i.e., varying fiber directions). Therefore, in cases such as the SLB specimen, where the delamination is located at or near the specimen mid-plane, the ply orientation difference across a crack front might not cause inaccuracies when using laminate shell elements. Further investigation is warranted on the enriched shell element's performance for bimaterial crack problems where the delaminations are not located near the mid-plane.

Based on Figure 27, a mesh size corresponding to a $\Delta a/h'$ ratio range of 0.49-2.46 can predict accurate energy release rates in the enriched element for a mixed-mode bimaterial delamination that has similar laminate stiffness on either side of the crack.

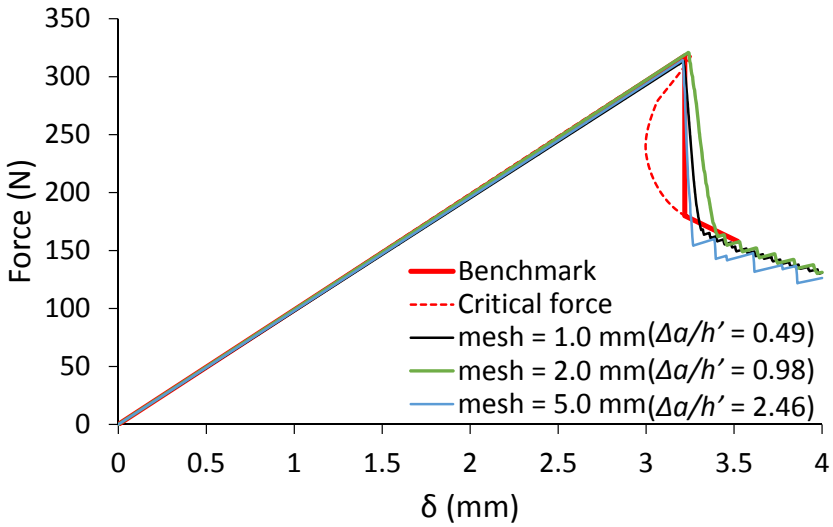

Figure 27. SLB: Force-displacement data correlation, $G_{II}/G_T = 0.4$.

4.2 Experimental Validation: Delamination-migration test and model description

Ratcliffe et al. [75] developed a test in which delamination-migration could be observed in detail in a cross-ply specimen. A schematic of the test is shown in Figure 28a. A test specimen with a pre-existing crack is clamped at both ends and pin-loaded normal to the specimen surface. After the pre-existing crack grows and reaches a certain length past the load application point, migration occurs and the delamination continues at a new interface (see Figure 28b). The delamination-migration experiment is useful for model validation because it isolates in a clear manner one specific damage mechanism that can occur as part of a larger complex progressive damage process. De Carvalho et al. [47] successfully simulated the experiment in a plane-strain high fidelity model.

A model was created using the enriched shell element to simulate the delamination-migration experiment. One mesh size of 1.0 mm was considered. A schematic of the model is shown in Figure 29. The rotational springs at the clamp boundaries were calibrated using Digital Image Correlation (DIC) data from the deformed specimen shape in a test where no damage occured. In the shell model, the rotational spring stiffnesses, k_{s1} and k_{s2}, were adjusted via trial and error until both the overall specimen deflected shape and the slope of the linear-elastic force-displacement curve matched that of the test. $G_c^{(tr)}$ was defined in this case as equal to the G_{Ic} value for the matrix. Material properties used in the delamination-migration model are

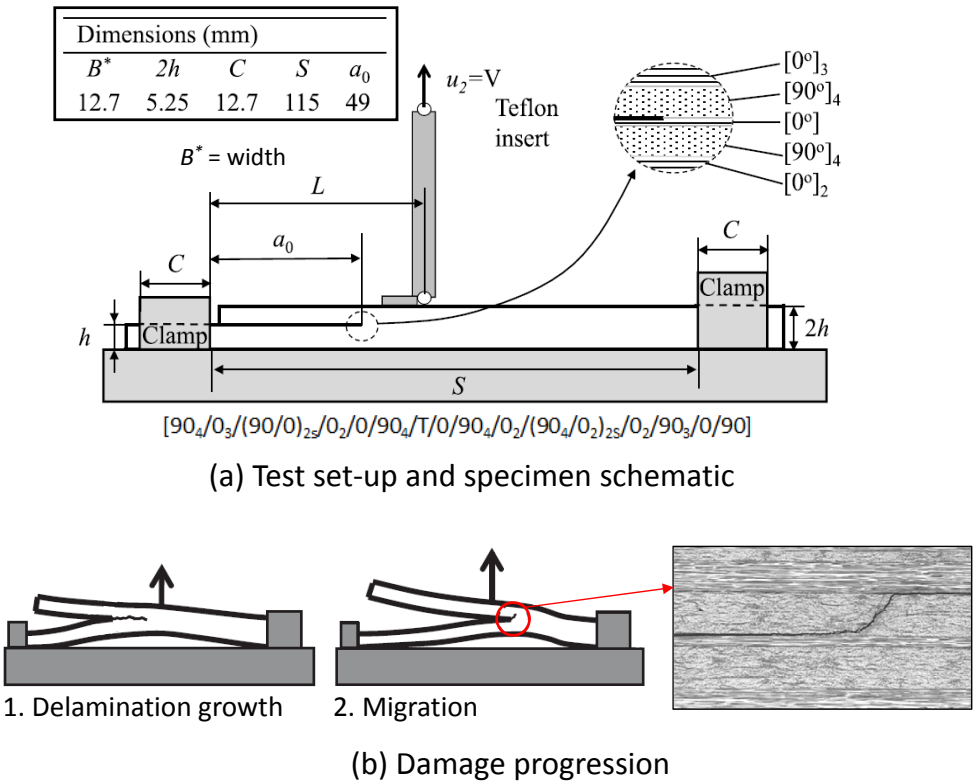

Figure 28. Delamination-migration test summary [47].

given in Table 1.

4.3 Experimental Validation: Results and Discussion

Force-displacement correlation for the delamination-migration test is shown in Figure 30 for three specimen configurations with different load application points, L (see Figure 28). While generally a close agreement between the shell model results and the experimental data for critical load and displacement is seen, the shell model accuracy decreases as L approaches a_o. A possible explanation for this decrease in accuracy is that when the load is applied directly above or near the crack tip, the stresses near the crack tip influencing growth are then a result of both global structural deflection and local deformation due to the load application nearby. The shell model may not be well suited for problems of this nature because there is not a three-dimensional stress field determined in the element formulation to account for applied local deformations. Nevertheless, the point of initiation of unstable damage growth and the occurrence of migration are both generally predicted well by the shell element models. These comparisons indicate that the assumptions for the migration prediction described in Section 3.2.2 are valid, but, as in any finite element

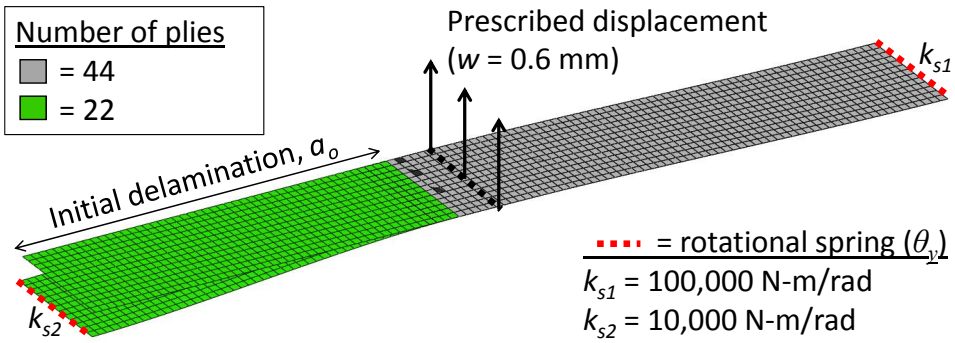

Figure 29. Delamination-migration: Enriched shell finite element model of delamination-migration test (Figures from [47]).

analysis, care should be taken to ensure that a shell is the right element choice for a given problem.

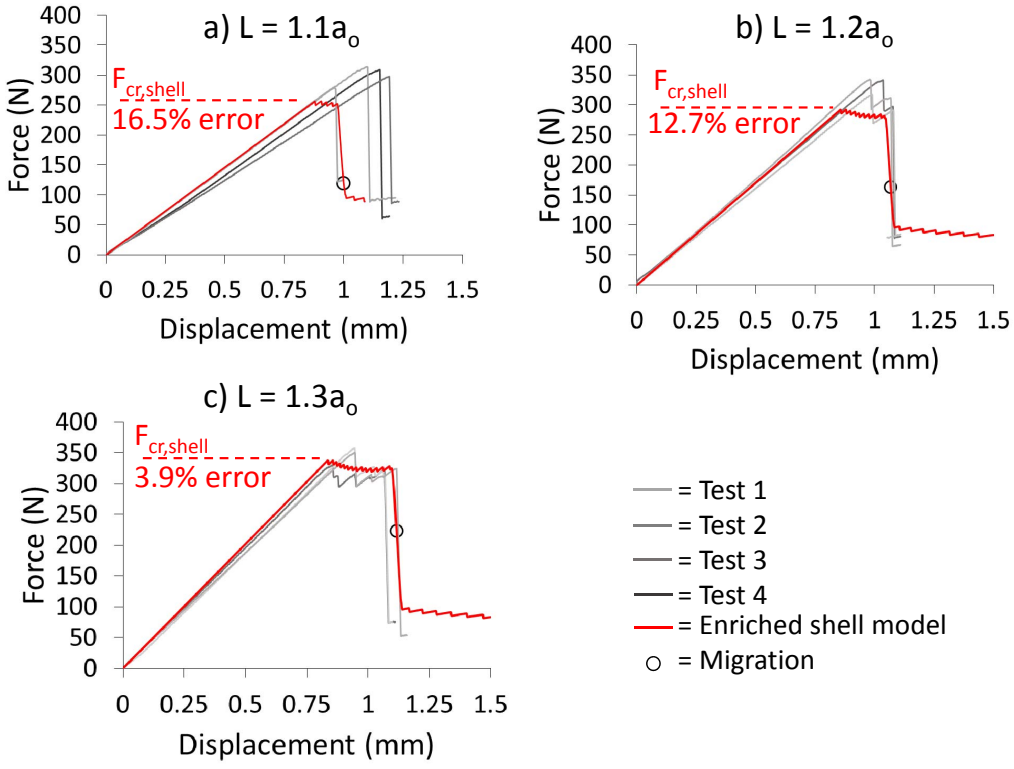

Figure 30. Delamination-migration: Force-displacement correlation (error compared to average of experimental curves).

Another correlation metric examined, in addition to force-displacement, was the location of migration onset, x_{mig}. Figure 31 shows the enriched shell model at the beginning and end of the load application. Using the color code as an indication of number of plies (i.e., thickness) of an element, the delamination is seen to first grow at the original interface until it reached the location x_{mig}, where it migrated through four plies to a new interface and then continued to grow. Beyond x_{mig}, the delamination is no longer at the midplane of the specimen and thus the thicknesses of the laminates on either side are no longer equal. Element thickness is represented as number of plies by the colors in Figure 31b. A summary of the migration location data from the experiment and the simulation is given in Table 4. Based on the correlation shown in Figures 30 and 31, the enriched shell is capable of simulating the delamination-migration experiment and potentially simulating additional three-dimensional damage processes that contain migration (i.e., such as Figure 1).

Table 4. Delamination-migration: Migration location correlation summary.

	x_{mig} (mm)		
	L = $1.1a_o$	L = $1.2a_o$	L = $1.3a_o$
Enriched shell	70.0	73.0	77.0
Experiment	66.0	67.5	71.5
Error	5.7%	7.5%	7.1%

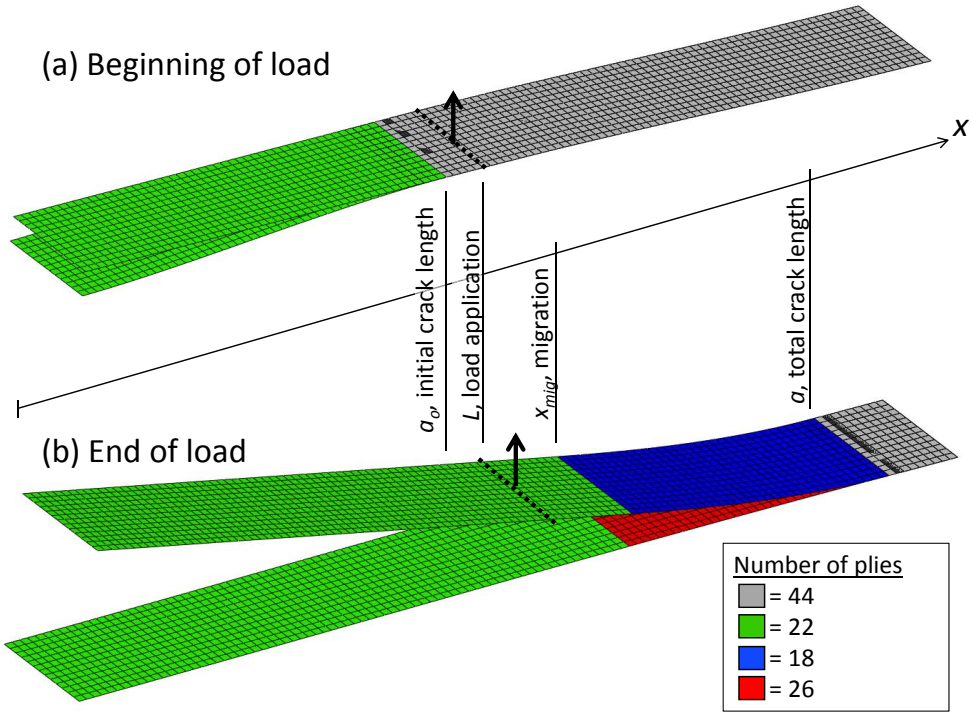

Figure 31. Delamination-migration: Migration location correlation.

5 Conclusion

A formulation was presented for a novel enriched shell finite element intended for use in progressive damage simulation in composite laminates. Using an adaptive fidelity type approach, the Virtual Crack Closure Technique is combined with the Floating Node Method to simulate delamination growth at an arbitrary ply interface in a laminate layup. A straightforward prediction technique for delamination-migration, along with a means to represent transverse damage features in a single layer shell element model, are included in the simulation capability. The formulation and results presented serve as the first milestone in development of an enriched shell element for three-dimensional progressive damage simulation in laminates.

The enriched shell element was verified for delamination simulation by comparing results against four numerical benchmark studies. DCB, ENF, MMB, and SLB specimens were used to verify Mode I, Mode II, Mixed-Mode I/II, and bimaterial delamination conditions. In all cases, the enriched element was shown to exhibit mesh independence in terms of stiffness and in terms of energy release rate prediction. Additionally, meshes sized to a crack-extension-length to laminate thickness ratio, $\Delta a/h'$, of approximately 0.5-2.2 were shown to result in accurate damage simulation behavior in all cases. It was found that, to ensure accurate stiffness, especially in Mode I conditions, several elements ahead of a delamination front must

be split with all nodes tied together enforcing translational DOF only (i.e., rotations are released). Concerning bimaterial cracks, the enriched shell performed well for the case considered with a +/- 30° delamination interface at the laminate midplane. Further investigation is warranted on the enriched shell element's ability to simulate bimaterial cracks, particularly for cases when the delamination is not located on or near the laminate midplane.

The enriched shell element was experimentally validated using test data from an experiment where delamination-migration could be observed. Stiffness and damage behavior predicted by the shell element both matched well with the experimental data. These results indicated that the enriched shell element is capable of accurately simulating a simple three-dimensional progressive damage process that includes delamination and delamination-migration via transverse matrix cracks.

References

1. S. Abrate. *Impact on composite structures*. Cambridge University Press, 2005.

2. S. Sánchez-Sáez, E. Barbero, R. Zaera, and C. Navarro. Compression after impact of thin composite laminates. *Composites Science and Technology*, 65(13):1911–1919, 2005.

3. C. Soutis and P.T. Curtis. Prediction of the post-impact compressive strength of CFRP laminated composites. *Composites Science and Technology*, 56(6):677–684, 1996.

4. M. De Freitas and L. Reis. Failure mechanisms on composite specimens subjected to compression after impact. *Composite Structures*, 42(4):365–373, 1998.

5. M.J. Hinton, A.S. Kaddour, and P.D. Soden. The world-wide failure exercise: Its origin, concept and content. In *Failure criteria in fiber reinforced polymer composites: the world wide failure exercise*, pages 2–28. Elsevier, Amsterdam, 2004.

6. A.S. Kaddour, M.J. Hinton, P.A. Smith, and S. Li. The background to the third world-wide failure exercise. *Journal of Composite Materials*, 47(20-21):2417–2426, 2013.

7. C.A. Rose, C.G. Dávila, and F.A. Leone. *Analysis methods for progressive damage of composite structures, NASA/TM 2013-218024*. NASA, 2013.

8. M. McElroy, J. Ratcliffe, M. Czabaj, J. Wang, and F.G. Yuan. A numerical and experimental study of damage growth in a composite laminate (paper no. 281). In *Proceedings of the American Society for Composites: 29th Technical Conference*, La Jolla, California, September 8-10, 2014. American Society for Composites.

9. W.J. Cantwell and J. Morton. The impact resistance of composite materials–a review. *Composites*, 22(5):347–362, 1991.

10. A.L. Dobyns and T.R. Porter. A study of the structural integrity of graphite composite structure subjected to low velocity impact. *Polymer Engineering & Science*, 21(8):493–498, 1981.

11. W. Elber. *Failure mechanics in low-velocity impacts on thin composite plates, NASA/TP 2152*. NASA, 1983.

12. H.Y. Choi, R.J. Downs, and F.K. Chang. A new approach toward understanding damage mechanisms and mechanics of laminated composites due to low-velocity impact: Part I - experiments. *Journal of Composite Materials*, 25(8):992–1011, 1991.

13. K.N. Shivakumar, W. Elber, and W. Illg. *Prediction of impact force and duration during low velocity impact on circular composite laminates, NASA Technical Memorandum 85703*. NASA, 1983.

14. R. Olsson. *Impact response of composite laminates - A guide to closed form solutions. FFA TN 1992-33*. The Aeronautical Institute of Sweden, 1993.

15. R. Olsson. Impact response of orthotropic composite plates predicted from a one-parameter differential equation. *AIAA Journal*, 30(6):1587–1596, 1992.

16. I.H. Choi and C.S. Hong. New approach for simple prediction of impact force history on composite laminates. *AIAA Journal*, 32(10):2067–2072, 1994.

17. R. Olsson. Analytical prediction of large mass impact damage in composite laminates. *Composites Part A: Applied Science and Manufacturing*, 32(9):1207–1215, 2001.

18. R. Olsson, M.V. Donadon, and B.G. Falzon. Delamination threshold load for dynamic impact on plates. *International Journal of Solids and Structures*, 43(10):3124–3141, 2006.

19. G.A.O. Davies and X. Zhang. Impact damage prediction in carbon composite structures. *International Journal of Impact Engineering*, 16(1):149–170, 1995.

20. P. Sjoblom. Simple design approach against low-velocity impact damage. *Advanced Materials Technology '87*, pages 529–539, 1987.

21. H.Y. Choi and F.K. Chang. A model for predicting damage in graphite/epoxy laminated composites resulting from low-velocity point impact. *Journal of Composite Materials*, 26(14):2134–2169, 1992.

22. G.A.O. Davies and P. Robinson. Predicting failure by debonding/delamination. *AGARD, Debonding/Delamination of Composites*, 1992.

23. F. Collombet, X. Lalbin, and J.L. Lataillade. Impact behavior of laminated composites: physical basis for finite element analysis. *Composites Science and Technology*, 58(3):463–478, 1998.

24. P.H. Geubelle and J.S. Baylor. Impact-induced delamination of composites: a 2D simulation. *Composites Part B: Engineering*, 29(5):589–602, 1998.

25. G.I. Barenblatt. The formation of equilibrium cracks during brittle fracture. General ideas and hypotheses. Axially-symmetric cracks. *Journal of Applied Mathematics and Mechanics*, 23(3):622–636, 1959.

26. G. Bfer. An isoparametric joint/interface element for finite element analysis. *International Journal for Numerical Methods in Engineering*, 21(4):585–600, 1985.

27. P.P. Camanho, C.G. Davila, and M.F. De Moura. Numerical simulation of mixed-mode progressive delamination in composite materials. *Journal of Composite Materials*, 37(16):1415–1438, 2003.

28. A. Turon, P.P. Camanho, J. Costa, and C.G. Dávila. A damage model for the simulation of delamination in advanced composites under variable-mode loading. *Mechanics of Materials*, 38(11):1072–1089, 2006.

29. R. Krueger. Virtual crack closure technique: history, approach, and applications. *Applied Mechanics Reviews*, 57(2):109–143, 2004.

30. E.F. Rybicki and M.F. Kanninen. A finite element calculation of stress intensity factors by a modified crack closure integral. *Engineering Fracture Mechanics*, 9(4):931–938, 1977.

31. G.R. Irwin. Fracture. *Handbuch der Physik*, III, 1958.

32. E.F. Rybicki, D.W. Schmueser, and J. Fox. An energy release rate approach for stable crack growth in the free-edge delamination problem. *Journal of Composite Materials*, 11(4):470–487, 1977.

33. T.K. O'Brien. Characterization of delamination onset and growth in a composite laminate. *Damage in Composite Materials, ASTM STP*, 775(2):140–167, 1982.

34. M.R. Wisnom. Modelling discrete failures in composites with interface elements. *Composites Part A: Applied Science and Manufacturing*, 41(7):795–805, 2010.

35. P.F. Liu and J.Y. Zheng. Recent developments on damage modeling and finite element analysis for composite laminates: a review. *Materials & Design*, 31(8):3825–3834, 2010.

36. A. Matzenmiller, J. Lubliner, and R.L. Taylor. A constitutive model for anisotropic damage in fiber-composites. *Mechanics of Materials*, 20(2):125–152, 1995.

37. P. Maimí, P.P. Camanho, J.A. Mayugo, and C.G. Dávila. A continuum damage model for composite laminates: Part I - constitutive model. *Mechanics of Materials*, 39(10):897–908, 2007.

38. P. Maimí, P.P. Camanho, J.A. Mayugo, and C.G. Dávila. A continuum damage model for composite laminates: Part II - computational implementation and validation. *Mechanics of Materials*, 39(10):909–919, 2007.

39. T. Belytschko and T. Black. Elastic crack growth in finite elements with minimal remeshing. *International Journal for Numerical Methods in Engineering*, 45(5):601–620, 1999.

40. N. Moes, J. Dolbow, and T. Belytschko. A finite element method for crack growth without remeshing. *International Journal for Numerical Methods in Engineering*, 46(1):131–150, 1999.

41. E.V. González, P. Maimí, P.P. Camanho, A. Turon, and J.A. Mayugo. Simulation of drop-weight impact and compression after impact tests on composite laminates. *Composite Structures*, 94(11):3364–3378, 2012.

42. Y. Shi, T. Swait, and C. Soutis. Modelling damage evolution in composite laminates subjected to low velocity impact. *Composite Structures*, 94(9):2902–2913, 2012.

43. D. Feng and F. Aymerich. Finite element modelling of damage induced by low-velocity impact on composite laminates. *Composite Structures*, 108:161–171, 2014.

44. E.V. Iarve, M.R. Gurvich, D.H. Mollenhauer, C.A. Rose, and C.G. Dávila. Mesh-independent matrix cracking and delamination modeling in laminated composites. *International Journal for Numerical Methods in Engineering*, 88(8):749–773, 2011.

45. M.J. Swindeman, E.V. Iarve, R.A. Brockman, D.H. Mollenhauer, and S.R. Hallett. Strength prediction in open hole composite laminates by using discrete damage modeling. *AIAA Journal*, 51(4):936–945, 2013.

46. Z.Q. Zhou, X.J. Fang, B.N. Cox, and Q.D. Yang. The evolution of a transverse intra-ply crack coupled to delamination cracks. *International Journal of Fracture*, 165(1):77–92, 2010.

47. N.V. De Carvalho, B.Y. Chen, S.T. Pinho, J.G. Ratcliffe, P.M. Baiz, and T.E. Tay. Modeling delamination migration in cross-ply tape laminates. *Composites Part A: Applied Science and Manufacturing*, 71:192–203, 2015.

48. A.C. Orifici, R.S. Thomson, R. Degenhardt, C. Bisagni, and J. Bayandor. Development of a finite-element analysis methodology for the propagation of delaminations in composite structures. *Mechanics of Composite Materials*, 43(1):9–28, 2007.

49. F.P. Van der Meer, L.J. Sluys, S.R. Hallett, and M.R. Wisnom. Computational modeling of complex failure mechanisms in laminates. *Journal of Composite Materials*, 46(5):603–623, 2012.

50. C. Bouvet, S. Rivallant, and J.J. Barrau. Low velocity impact modeling in composite laminates capturing permanent indentation. *Composites Science and Technology*, 72(16):1977–1988, 2012.

51. S.P. Engelstad, R.J. Stover, and J.E. Action. *Air Vehicle Integration and Technology Research (AVIATR) Task Order 0037: Assessment, Quantification, and Benefits of Applying Damage Tolerant Design Principles to Advanced Composite Aircraft Structure AFRL-RQ-WP-TR-2015-0068*. AFRL, 2015.

52. R. Krueger and T.K. O'Brien. A shell/3D modeling technique for the analysis of delaminated composite laminates. *Composites Part A: Applied Science and Manufacturing*, 32(1):25–44, 2001.

53. S. Heimbs, S. Heller, and P. Middendorf. Simulation of low velocity impact on composite plates with compressive preload. In *7th German LS-DYNA Forum*, Bamberg, Germany, September, 2008.

54. S. Heimbs, S. Heller, P. Middendorf, F. Hähnel, and J. Weiße. Low velocity impact on CFRP plates with compressive preload: Test and modelling. *International Journal of Impact Engineering*, 36(10):1182–1193, 2009.

55. H. Qiao, W.Q. Chen, Q.D. Yang, and J. Lua. Augmented cohesive elements for efficient delamination analyses of composite laminates. *Journal of Engineering Materials and Technology*, 133(4):041010, 2011.

56. C.G. Dávila, P.P. Camanho, and A. Turon. Effective simulation of delamination in aeronautical structures using shells and cohesive elements. *Journal of Aircraft*, 45(2):663–672, 2008.

57. S. Zheng and C.T. Sun. A double-plate finite-element model for the impact-induced delamination problem. *Composites Science and Technology*, 53(1):111–118, 1995.

58. J.T. Wang, I.S. Raju, and D.W. Sleight. Composite skin-stiffener debond analyses using fracture mechanics approach with shell elements. *Composites Engineering*, 5(3):277–296, 1995.

59. J.T. Wang and I.S. Raju. Strain energy release rate formulae for skin-stiffener debond modeled with plate elements. *Engineering Fracture Mechanics*, 54(2):211–228, 1996.

60. E.H. Glaessgen, W.T. Riddell, and I.S. Raju. Nodal constraint, shear deformation and continuity effects related to the modeling of debonding of laminates, using plate elements. *Computer Modeling in Engineering and Sciences*, 3(1):103–116, 2002.

61. R. Krueger, K. Shivakumar, and I.S. Raju. Fracture mechanics analyses for interface crack problems: A review. In *Proceedings of the 54th AIAA/ASME/ASCE/AHS/ASC Structures, Structural Dynamics, and Materials Conference*, 2013.

62. R. Larsson. A discontinuous shell-interface element for delamination analysis of laminated composite structures. *Computer Methods in Applied Mechanics and Engineering*, 193(30):3173–3194, 2004.

63. J. Brouzoulis and M. Fagerström. Modelling of multiple delaminations in shells using XFEM. In *Proceedings for the 19th International Conference on Composite Materials (ICCM19)*, 2013.

64. J. Brouzoulis and M. Fagerström. An enriched shell element formulation for efficient modeling of multiple delamination propagation in laminates. *Composite Structures*, 126:196–206, 2015.

65. J. Brouzoulis, M. Fagerström, and E. Svenning. An enriched shell element formulation for modeling of inter- and intralaminar crack propagation in laminates. *Composite Structures*, 136:616–625, 2016.

66. E.V. Iarve. Mesh independent modelling of cracks by using higher order shape functions. *International Journal for Numerical Methods in Engineering*, 56(6):869–882, 2003.

67. F.P. Van der Meer and L.J. Sluys. A phantom node formulation with mixed mode cohesive law for splitting in laminates. *International Journal of Fracture*, 158(2):107–124, 2009.

68. B.Y. Chen, S.T. Pinho, N.V. De Carvalho, P.M. Baiz, and T.E. Tay. A floating node method for the modelling of discontinuities in composites. *Engineering Fracture Mechanics*, 127:104–134, 2014.

69. F.P. Van der Meer, L.J. Sluys, and N. Moës. Toward efficient and robust computation of energy release rate and mode mix for delamination. *Composites Part A: Applied Science and Manufacturing*, 43(7):1101–1112, 2012.

70. V.N. Burlayenko and T. Sadowski. FE modeling of delamination growth in interlaminar fracture specimens. *Budownictwo i Architektura*, 2:95–109, 2008.

71. D. Xie and S.B. Biggers Jr. Strain energy release rate calculation for a moving delamination front of arbitrary shape based on the virtual crack closure technique. Part I: Formulation and validation. *Engineering Fracture Mechanics*, 73:771–785, 2006.

72. D. Xie and S.B. Biggers Jr. Strain energy release rate calculation for a moving delamination front of arbitrary shape based on the virtual crack closure technique. Part II: Sensitivity study on modeling details. *Engineering Fracture Mechanics*, 73:786–801, 2006.

73. X. Li, C. Ferrie, E. Nottorf, and M. Portanova. Virtual crack closure technique on stepped crack front (VCCT-S). In *The American Helicopter Society 64th Annual Forum*, Montreal, Canada, April 29-May 1, 2013.

74. Y.P. Liu, C.Y. Chen, and G.O. Li. A modified zigzag approach to approximate moving crack front with arbitrary shape. *Engineering Fracture Mechanics*, 79:234–251, 2011.

75. J.G. Ratcliffe, M.W. Czabaj, and T.K. O'Brien. *A test for characterizing delamination migration in carbon/epoxy tape laminates NASA/TM-2013-218028*. NASA, 2013.

76. N.V. De Carvalho, B.Y. Chen, S.T. Pinho, P.M. Baiz, J.G. Ratcliffe, and T.E. Tay. *Floating node method and virtual crack closure technique for modeling matrix cracking-delamination interaction, NASA/CR-2013-218022*. NASA, 2013.

77. E.S. Greenhalgh, C. Rogers, and P. Robinson. Fractographic observations on delamination growth and the subsequent migration through the laminate. *Composites Science and Technology*, 69(14):2345–2351, 2009.

78. C. Canturri, E.S. Greenhalgh, S.T. Pinho, and J. Ankersen. Delamination growth directionality and the subsequent migration processes–the key to damage tolerant design. *Composites Part A: Applied Science and Manufacturing*, 54:79–87, 2013.

79. E.S. Greenhalgh, C. Canturri, and S.T. Pinho. A methodology for realistic delamination growth prediction based on fractographic observations. In *Proceedings of the American Society for Composites: 29th Technical Conference*, La Jolla, California, September 8-10, 2014.

80. H. Suemasu and Y. Tanikado. Damage growth behavior and interlaminar fracture resistance of CFRP laminates under shear fracture mode. *Advanced Composite Materials*, (accepted for publication):1–16, 2014.

81. Dassault Systems. *Abaqus 6.13 Analysis User Manual*. 2013.

82. E. Oñate. *Structural Analysis with the Finite Element Method. Linear Statics: Volume 2: Beams, Plates and Shells*. Springer Science and Business Media, 2013.

83. M. Laitinen, H. Lahtinen, and S.G. Sjölind. Transverse shear correction factors for laminates in cylindrical bending. *Communications in Numerical Methods in Engineering*, 11(1):41–47, 1995.

84. Stefanos Vlachoutsis. Shear correction factors for plates and shells. *International Journal for Numerical Methods in Engineering*, 33(7):1537–1552, 1992.

85. E. Oñate, O.C. Zienkiewicz, B. Suarez, and R.L. Taylor. A general methodology for deriving shear constrained Reissner-Mindlin plate elements. *International Journal for Numerical Methods in Engineering*, 33(2):345–367, 1992.

86. M.L. Benzeggagh and M. Kenane. Measurement of mixed-mode delamination fracture toughness of unidirectional glass/epoxy composites with mixed-mode bending apparatus. *Composites Science and Technology*, 56(4):439–449, 1996.

87. T.K. O'Brien. Composite interlaminar shear fracture toughness, G_{IIc}: Shear measurement or sheer myth? *ASTM Special Technical Publication*, 1330:3–18, 1998.

88. M. McElroy, F. Leone, J. Ratcliffe, M. Czabaj, and F.G. Yuan. Simulation of delamination–migration and core crushing in a CFRP sandwich structure. *Composites Part A: Applied Science and Manufacturing*, 79:192–202, 2015.

89. R. Krueger. A summary of benchmark examples to assess the performance of quasi-static delamination propagation prediction capabilities in finite element codes. *Journal of Composite Materials*, 49:3297–3316, 2015.

90. B. Cotterell, K. Hbaieb, J.G. Williams, H. Hadavinia, and V. Tropsa. The root rotation in double cantilever beam and peel tests. *Mechanics of Materials*, 38(7):571–584, 2006.

91. C.T. Sun and Z.H. Jin. *Fracture Mechanics*. Elsevier, 2012.

REPORT DOCUMENTATION PAGE

Form Approved
OMB No. 0704-0188

The public reporting burden for this collection of information is estimated to average 1 hour per response, including the time for reviewing instructions, searching existing data sources, gathering and maintaining the data needed, and completing and reviewing the collection of information. Send comments regarding this burden estimate or any other aspect of this collection of information, including suggestions for reducing the burden, to Department of Defense, Washington Headquarters Services, Directorate for Information Operations and Reports (0704-0188), 1215 Jefferson Davis Highway, Suite 1204, Arlington, VA 22202-4302. Respondents should be aware that notwithstanding any other provision of law, no person shall be subject to any penalty for failing to comply with a collection of information if it does not display a currently valid OMB control number.
PLEASE DO NOT RETURN YOUR FORM TO THE ABOVE ADDRESS.

1. REPORT DATE *(DD-MM-YYYY)*	2. REPORT TYPE	3. DATES COVERED *(From - To)*
01- 06 - 2016	Technical Publication	

4. TITLE AND SUBTITLE

An Enriched Shell Finite Element for Progressive Damage Simulation in Composite Laminates

5a. CONTRACT NUMBER

5b. GRANT NUMBER

5c. PROGRAM ELEMENT NUMBER

6. AUTHOR(S)

McElroy, Mark W.

5d. PROJECT NUMBER

5e. TASK NUMBER

5f. WORK UNIT NUMBER

826611.04.07.01

7. PERFORMING ORGANIZATION NAME(S) AND ADDRESS(ES)

NASA Langley Research Center
Hampton, VA 23681-2199

8. PERFORMING ORGANIZATION REPORT NUMBER

L-20716

9. SPONSORING/MONITORING AGENCY NAME(S) AND ADDRESS(ES)

National Aeronautics and Space Administration
Washington, DC 20546-0001

10. SPONSOR/MONITOR'S ACRONYM(S)

NASA

11. SPONSOR/MONITOR'S REPORT NUMBER(S)

NASA-TP-2016-219211

12. DISTRIBUTION/AVAILABILITY STATEMENT

Unclassified - Unlimited
Subject Category 24
Availability: NASA STI Program (757) 864-9658

13. SUPPLEMENTARY NOTES

14. ABSTRACT

The paper covers the early development of an enriched shell finite element for damage simulation in composite laminates.

15. SUBJECT TERMS

Composite; Delamination progressive damage; Shell element

16. SECURITY CLASSIFICATION OF:			17. LIMITATION OF ABSTRACT	18. NUMBER OF PAGES	19a. NAME OF RESPONSIBLE PERSON
a. REPORT	b. ABSTRACT	c. THIS PAGE			STI Help Desk (email: help@sti.nasa.gov)
U	U	U	UU	58	19b. TELEPHONE NUMBER *(Include area code)* (757) 864-9658